

# ADHESIVE ROUGH SURFACE CONTACT

by

**Clint Adam Morrow**

B.S., University of Kentucky, 1996

M.S., University of Kentucky, 1999

Submitted to the Graduate Faculty of  
the School of Engineering in partial fulfillment  
of the requirements for the degree of

**Doctor of Philosophy**

University of Pittsburgh

2003

UNIVERSITY OF PITTSBURGH  
SCHOOL OF ENGINEERING

This dissertation was presented

by

Clint Adam Morrow

It was defended on

November 20, 2003

and approved by

Michael R. Lovell, Associate Professor, Mechanical Eng. Dept.

Scott X. Mao, Professor, Mechanical Eng. Dept.

William S. Slaughter, Associate Professor, Mechanical Eng. Dept.

Frederick S. Pettit, Professor, Material Science Dept.

Dipo Onipede Jr., Mechanical Eng. Dept., Pennsylvania State University

Dissertation Director: Michael R. Lovell, Associate Professor, Mechanical Eng. Dept.

# ADHESIVE ROUGH SURFACE CONTACT

Clint Adam Morrow, PhD

University of Pittsburgh, 2003

The focus of this dissertation is to use analytical and numerical methods to determine mechanisms which increase or decrease the adherence force between micro-scale components. Several different methods are used to accomplish this task: 1) a traditional statistical approach is used to analytically determine the adherence force as a function of surface roughness; 2) a semi-analytical solution is developed for the adhesion of isotropic rough surfaces; 3) a numerical approach utilizes a three-dimensional surface characterization to determine adherence force trends with respect to roughness and material parameters; 4) combining a micro-scaled friction model with item 3), static friction forces are determined as a function of material parameters as well as surface roughness. To inspire further rough surface solutions, an adhesive solution for cylinders is extended to include the solution regime for when there is no longer intimate contact, but adhesive forces are still active. For each of these methodologies there are advantages and disadvantages which arise from the assumptions made in constructing the solution, which are subsequently discussed.

## TABLE OF CONTENTS

<b>PREFACE</b> . . . . .	ix
<b>1.0 INTRODUCTION</b> . . . . .	1
1.1 MOTIVATION . . . . .	2
1.2 OBJECTIVES AND METHODOLOGY . . . . .	4
1.3 LITERATURE REVIEW . . . . .	7
<b>2.0 SINGLE ASPERITY CONTACT</b> . . . . .	11
2.1 ADHESIVE THEORY OF JOHNSON KENDALL, & ROBERTS (JKR) . . . . .	11
2.2 JKR-DMT TRANSITION SOLUTION WITH KIM EXTENSION . . . . .	14
2.3 ADHESION OF ELASTIC CYLINDERS . . . . .	16
2.3.1 BANEY AND HUI SOLUTION . . . . .	18
2.3.2 ANALYTICAL EXTENTION TO BANEY-HUI SOLUTION . . . . .	22
<b>3.0 G-W TYPE TRANSITION SOLUTION FOR ROUGH SURFACES</b> . . . . .	26
3.1 INTRODUCTION . . . . .	26
3.2 BACKGROUND . . . . .	26
3.3 APPROXIMATION OF MAUGIS' TRANSITION SOLUTION . . . . .	27
3.4 METHODOLOGY FOR ADHESIVE ROUGH SOLUTION . . . . .	31
3.5 RESULTS . . . . .	34
3.6 SUMMARY AND DISSCUSSION . . . . .	35
<b>4.0 FRACTAL MODEL FOR ADHESIVE CONTACT OF JKR TYPE</b> . . . . .	37
4.1 INTRODUCTION . . . . .	37
4.2 BACKGROUND . . . . .	37
4.3 FRACTAL SURFACE CHARACTERIZATION . . . . .	38

4.4	ADHESIVE FRACTAL CONTACT MODEL . . . . .	42
4.5	RESULTS AND DISCUSSION . . . . .	47
4.6	SUMMARY AND CONCLUSIONS . . . . .	53
<b>5.0</b>	<b>FRACTAL CONTACT MODEL FOR JKR-DMT SOLUTION REGIME</b>	<b>54</b>
5.1	INTRODUCTION . . . . .	54
5.2	3-D ROUGH SURFACE SIMULATION . . . . .	54
5.3	ADHESIVE ROUGH SURFACE SOLUTION METHODOLOGY . . . . .	61
5.3.1	BACKGROUND . . . . .	61
5.3.2	ALGORITHM . . . . .	64
5.4	RESULTS . . . . .	65
5.5	CONCLUSIONS . . . . .	70
<b>6.0</b>	<b>SCALE DEPENDENT ADHESIVE FRICTION MODEL</b> . . . . .	<b>72</b>
6.1	INTRODUCTION . . . . .	72
6.2	HURTADO AND KIM MODEL . . . . .	72
6.2.1	CONCURRENT TO SINGLE-DISLOCATION-ASSISTED (SDA) SLIP	73
6.2.2	SDA SLIP TO MULTIPLE-DISLOCATION-COOPERATED (MDC)	
	SLIP . . . . .	74
6.3	HK IMPLEMENTATION . . . . .	75
6.4	RESULTS . . . . .	76
6.5	DISCUSSION . . . . .	78
	<b>APPENDIX. CURVE-FIT EQUATIONS</b> . . . . .	<b>80</b>
	<b>BIBLIOGRAPHY</b> . . . . .	<b>82</b>

## LIST OF TABLES

1	Contribution of this dissertation to single asperity adhesive contact. . . . .	5
2	Contributions of this dissertation to adhesive rough surface contact. . . . .	6
3	Single asperity and Rough Surface adhesive theories . . . . .	27
4	Values for curve-fit parameters for transition parameter values less than one (see Appendix A for values greater than one). . . . .	29
5	Rough surface contact theories. . . . .	37
6	Conditions for numerical results. . . . .	48
7	Operating conditions for the investigation of individual parameters. . . . .	67
8	The effect of varying $D$ on friction force, $G = 1.3152$ nm . . . . .	78
9	The effect of varying $G$ on friction force, $D = 2.7815$ . . . . .	79

## LIST OF FIGURES

1	‘Dimples’ used to keep separate neighboring micro-sized components. . . . .	3
2	Micro-steam engine makes use of adherence forces. . . . .	4
3	Dugdale and Lennard-Jones force separation laws. . . . .	9
4	Depiction of physical variables used in this section. . . . .	13
5	Intimate contact and adhesive radii. . . . .	15
6	Representation of parameters given by Kim <i>et al</i> extension. . . . .	16
7	Variation of non-dimensional contact radius with dimensionless approach for various values of the transition parameter. . . . .	17
8	Dimensionless plot showing load as a function of approach for various values of the transition parameter. . . . .	18
9	Geometry of the cylinders in contact. . . . .	20
10	Physical description of pressure distributions. . . . .	21
11	Intimate contact radius versus load. . . . .	23
12	Adhesive contact radius versus load. . . . .	25
13	The black curves represent the solution given from Maugis’ solution, and in white the curve-fit results are shown laid overtop. . . . .	29
14	Depiction of composite rough surface at a separation of $d$ . . . . .	31
15	Probability of an asperity being stretched or compressed. . . . .	33
16	Adherence force for rough surfaces for various values of the transition parameter. . . . .	34
17	Power spectrum of equivalent rough surface. . . . .	40
18	Geometry of contact spot with a given interference. . . . .	43
19	Truncated contact area depiction. . . . .	44

20	Load-Deflection curve for JKR theory . . . . .	46
21	Effect of fractal parameter $D$ on pull-off force . . . . .	49
22	Fractal parameter $D=1.2$ . . . . .	49
23	Fractal parameter $D=1.4$ . . . . .	50
24	Effect of fractal parameter $G$ on pull-off force . . . . .	50
25	Effect of $G$ on surface topography. . . . .	51
26	Effect of varying effective elastic modulus, $K$ , on pull-off force . . . . .	52
27	Typical AFM scan of ribbed LIGA surface. . . . .	56
28	AFM scan of mating LIGA surface. . . . .	57
29	Contour plot of surface topography for simulated surface. . . . .	59
30	Axi-symmetric power distribution of simulated surface. . . . .	60
31	Iterative scheme to solve for total load and area. . . . .	63
32	Single asperity validation of algorithm. . . . .	66
33	Effect of varying stiffness on adherence force. . . . .	68
34	Effect of varying surface energy on adherence force. . . . .	68
35	Effect of varying fractal roughness parameter $D$ on adherence force. . . . .	69
36	Effect of varying fractal scaling parameter $G$ on adherence force. . . . .	70
37	HK scale depend friction model. . . . .	73
38	Model of dislocation loops. . . . .	74
39	The effect of varying the fractal roughness parameter on friction. . . . .	77
40	The effect of varying the fractal scaling parameter on friction. . . . .	79

## PREFACE

I would like to thank Dr. Michael Lovell for his advice, support and friendship during my studies here at the University of Pittsburgh. His countless hours spent reviewing drafts offering suggestions, and providing guidance has enabled me to reach this point. For all of his efforts in this research I offer him my deepest gratitude. For serving on my Dissertation committee, I would like to thank Dr. Scott Mao, Dr. William Slaughter, Dr. Frederick Pettit and Dr. Dipo Onipede. I also thank them for reviewing my work and offering their suggestions.

I would also like to thank, Dr. Xinguo Ning for his collaboration on the content in chapter 3. I am grateful to Dr. Reese Jones of Sandia National Labs in Livermore, California for him introducing to the area of adhesive contact and it's application to MEMS devices.

To my wife Charlotte, I would like to dedicate this work. Without out her love, support, and encouragement I would not have had this opportunity.

## 1.0 INTRODUCTION

Over the past decade, the design and utilization of micro-scale devices has continuously increased. The micro-chip has become an everyday component of modern society. Functionality is being extended to the micro-chip through the addition of micro-machines. These micro-machines are made up of micro-electro-mechanical systems (MEMS) which are being integrated with the electrical circuitry of the micro-chip. This powerful combination enables the chip to *sense* and *act* to a variety of outside stimuli. Many of the silicon based fabrication techniques originally used for micro-chips are now being used to construct MEMS components. More notably, LIGA technology has extended the range of fabrication materials to include metals such as nickel and copper. LIGA, is a german acronym for Lithographie Galvano-formun Abformung, or lithography, electroforming and molding. This process allows for the creation of micron sized features on metal parts. These micro-scaled manufacturing techniques are making MEMS implementation an attractive design alternative to conventional technology. As the manufacturing MEMS components becomes more practical, the utilization of micro-sized components will increase due to their numerous beneficial qualities that include: lower cost, reduced weight, and improved performance. More specifically, by decreasing the required number of parts and assembly time for a device, MEMS technology can often reduce the cost of manufacturing small-scale components. Likewise, through the reduction of the physical size and mass, MEMS technology can enhance the performance of actuator and transducer elements by minimizing inertial effects.

Although the benefits of implementing and utilizing MEMS technology seem almost obvious, the pitfalls are not as apparent. Devices that utilize MEMS technology will often have mating surfaces. The contact at the surface interface is governed by asperity interaction. This is due to the fact that moderate surface roughness and light loading conditions lead to

contact between neighboring asperities. Components that reach this size have a high surface to volume ratio which leaves them highly susceptible to surface forces. Stiction forces can arise from any number of phenomenon such as van der Waals, capillary, ionic and molecular forces. Since the adhesive forces tend to make neighboring surfaces ‘jump’ into contact, guides and separating mechanisms are added to the design of MEMS scale components to insure there is no unwanted contact, as shown in Figure (1) In some circumstances, adhesive forces are used to create a design advantage. The micro-sized steam engine shown in Figure (2), for example, uses capillary forces as a restoring force for the pistons.

Throughout this dissertation two similar sounding terms are going to be utilized when discussing attractive forces, they are, *adhesive forces* and the *adherence forces*. Adhesion forces refer to interacting forces between surfaces. Whereas the adherence (stiction) is defined as the minimum force required to separate two contacting surfaces. Adherence (or pull-off) force can be significantly influence by numerous parameters. Surface roughness, in example, may actually reduce the adherence force under certain conditions. For illustration purposes, consider a rough surface in contact with a flat plane. On the rough surface, some of the smaller asperities will be stretched by adhesion, while some of the taller ones will be compressed through contact. Depending on the conditions, the elastic energy in the taller asperities can in effect force apart the stretched smaller asperities, thereby reducing the overall adherence force. K.L. Johnson has referred to this phenomenon as the ‘elbowing effect’ [1]. This result highlights the primary focus of this work: to identify the mechanisms which effect the adherence force between surfaces in MEMS and other related devices and then to demonstrate how each mechanism effects the adherence force. To accomplish this task, a diverse set of solutions for adhesive rough surfaces is introduced.

## 1.1 MOTIVATION

In order to gain the full advantage of the beneficial performance characteristics offered by MEMS devices and chip-based micro-machines, it is necessary to obtain a complete understanding of how adhesive forces limit their functionality. Although there have been several adhesive theories offered for rough surfaces [2]-[3], each have their own limitations. This dis-

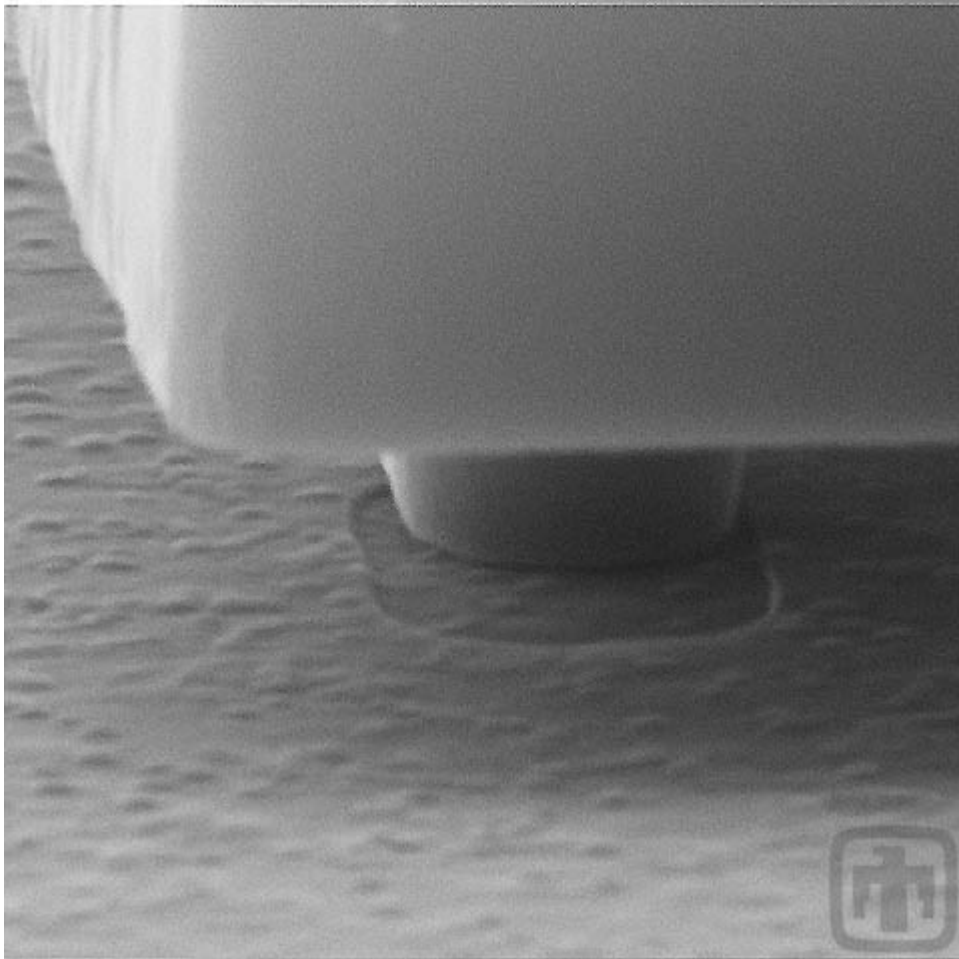


Figure 1: ‘Dimples’ used to keep separate neighboring micro-sized components. SANDIA NATIONAL LABS

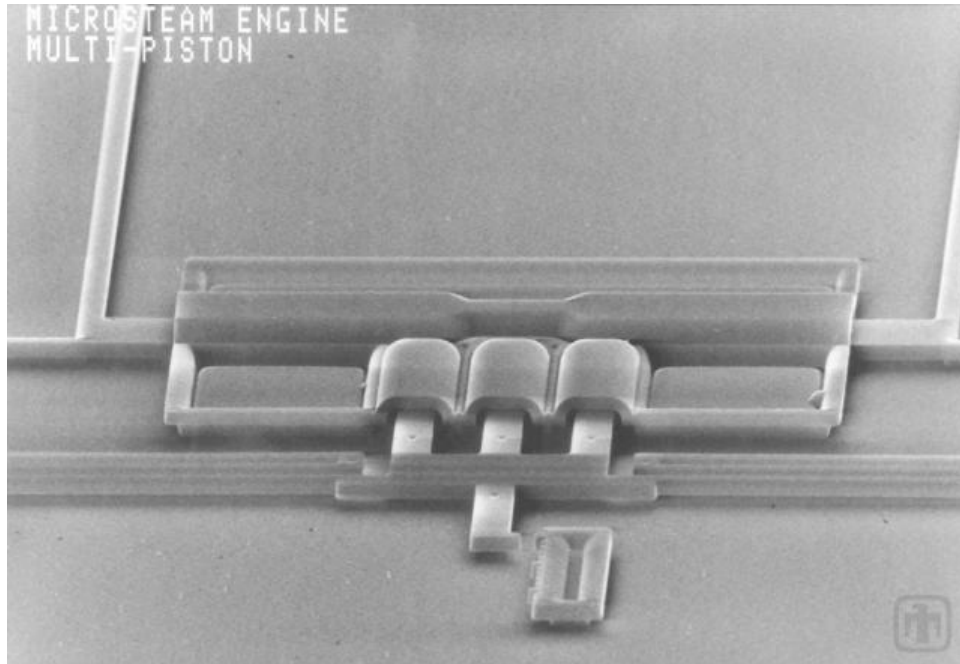


Figure 2: Micro-steam engine makes use of adherence forces. SANDIA NATIONAL LABS

sertation attempts to eliminate the drawbacks of the previous work by utilizing both scale dependent and scale independent characterizations with JKR theory [4] and the Maugis-Dugdale [5] adhesive solutions.

## 1.2 OBJECTIVES AND METHODOLOGY

This present research has three main objectives:

1. To develop methods to solve adhesive rough surface contact problems.
2. To identify and elucidate the effects of rough surface topography, interface stiffness, and surface energy on the adherence force of a contact interface.
3. To determine the adherence force during rough surface contact and to show how adhesion can effect frictional forces.

To achieve these objectives, several different novel contact mechanics problems will be solved. The overall contribution of this dissertation is described in Tables 1 and 2. In

Table 1: Contribution of this dissertation to single asperity adhesive contact.

Geometry	Theory/Solution	Description	Application
Elastic cylinders	Baney and Hui [6]	Complete adhesive contact regime	Adhesive contact of elastic cylinders
	Section (2.3)	Extends [6] solution to consider adhesive interaction where cylinders do not touch	Same as above
Elastic spheres	Johnson, Kendall, and Roberts [4]	soft solids, large radii and adhesive forces	Adhesive contact of elastic spheres
	DMT [7]	hard solids, small radii and adhesive forces	Same as above
	Maugis-Dugdale [5]	Adhesive regime between JKR and DMT theories	Same as above

Table 1, the available single asperity contact theories are described. In chapter 2 of this dissertation an adhesive contact model for cylinders has been extended [6] to include the solution regime when the two cylinders are no longer in physical contact but within the range of adhesion. This solution regime provides a foundation for further rough surface contact problems similar to that available for elastic spheres.

The contributions of the dissertation in the area of general rough surface contact is provided in Table 2. As shown in the table, four important contact problems have been added to this area. First, for a contact interface where the length scale is well known, a scale dependent approach is used in chapter 3 to determine the pull-off force for the Maugis-Dugdale (JKR-DMT transition) contact regime. This approach uses the Maugis-Dugdale solution for adhesive spheres coupled with a statistical surface characterization. In the case where the length scale is unknown, a fractal characterization is then applied in chapter 4 with the adhesive solution of Johnson, Kendall and Roberts (JKR) where the adhesive contact type is known a priori. A three-dimensional fractal model is subsequently developed chapter 5 which utilizes the Maugis-Dugdale solution for the case when neither the length scale and

Table 2: Contributions of this dissertation to adhesive rough surface contact.

Adhesive Rough Surface – Multi-Asperity contact	Fuller and Tabor [2]	Statistical surface characterization which uses JKR contact model	Contact where roughness is at a known length scale and contact type is predominately JKR
	Maugis [8]	Statistical surface characterization with DMT constitutive model	Same as above but contact type is assumed to be DMT
	Morrow, Lovell, and Ning [9], chapter 3	Statistical surface characterization which uses the Maugis-Dugdale model	Same as above but adhesive contact type is between JKR and DMT
	chapter 4	Fractal surface characterization which uses JKR constitutive model	Micro-sized contact areas where roughness is exhibited over several length scales and contact type is assumed JKR
	chapter 5	Fractal surface topography with JKR-DMT contact model	same as above but contact type between JKR and DMT
	chapter 6	same as above but with scale depend friction model included	same as above

the adhesive contact type is unknown a priori. This last solution is the most general of all solution methods and can be easily generalized to further solve anisotropic surface roughness. Using the results for the loading curve generated in chapter 5 a frictional force is determined chapter 6 utilizing a scale-based friction model for spheres in contact.

### 1.3 LITERATURE REVIEW

To better understand the context of the work introduced in this dissertation, it is important to provide an adequate background of the prior work performed in the area of adhesive rough surface contact. For determining the conditions under which the adherence force is increased or diminished, several rough surface solutions have been developed. Many of these theories idealize the asperity in contact as a spherical shape. Reviewing the literature, Johnson, Kendall, and Roberts (JKR) [4] found the first solution between elastic sphere using an energy balance approach. JKR determined the pull-off force to be  $(3/2)\pi wR$ , where  $w$  is the work of adhesion, and  $R$  is the effective radius. The work of adhesion is given by:

$$w = \gamma_1 + \gamma_2 - \gamma_{12} \tag{1.1}$$

where  $\gamma_1$  and  $\gamma_2$  represent the surface energy and  $\gamma_{12}$  is the interface energy. The effective radius is defined as:

$$R = \frac{R_1 R_2}{R_1 + R_2} \tag{1.2}$$

where  $R_1$  and  $R_2$  are the respective radii of each contacting sphere. Derjaguin, Muller and Toporov (DMT) [7] subsequently solved the same problem numerically and determined the pull-off force to be  $2\pi wR$ . A dispute began between the two groups that was finally resolved by Tabor [10], who determined the limiting assumptions in both theories. JKR assumed that the cohesive zone was infinitesimally small. The term cohesive zone refers to the area just outside the region of intimate contact that is subjected to adhesive traction. Likewise, DMT, assumed that in the cohesive zone did not alter the Hertzian profile. In his work, Tabor proposed that the DMT and JKR approaches were on opposite ends of

the solution spectrum. He introduced an adhesion (Tabor) parameter to characterize the transition between the JKR and DMT theories:

$$\mu \approx \left( \frac{w^2 R}{K^2 z_o^3} \right)^{1/3} \quad (1.3)$$

where  $z_o$  represents the interatomic spacing. In Equation (1.3), the effective elastic modulus  $K$  is given by:

$$\frac{1}{K} = \frac{3}{4} \left( \frac{1 - \nu_1^2}{E_1} + \frac{1 - \nu_2^2}{E_2} \right) \quad (1.4)$$

where  $E_1$ ,  $E_2$ ,  $\nu_1$ , and  $\nu_2$  represent the Young's modulus and Poisson's ratio for the respective spheres.

Tabor's theory was then numerically proven by Muller and others in [11]-[12]. Maugis [5] later offered an analytical solution which spanned the transition from JKR to DMT through his own transition parameter  $\lambda$ .

$$\lambda = \frac{2\sigma_o}{(\pi w K^2 / R)^{1/3}} \quad (1.5)$$

The parameter  $\sigma_o$  represents the constant traction that is active over a separation distance,  $h_o$ . This is called the Dugdale assumption and is graphically depicted in Figure (3). Therefore the Dugdale approximation was integral to Maugis' theory. Today some refer to this solution as the Maugis-Dugdale solution.

The theories of contacting spheres (or single asperity contacts) has long been a part of developing rough surface contact solutions. Perhaps the most notable example is the work of Greenwood and Williamson (GW) [13]. GW is a statistically based approach which determines the likelihood of an asperity being in contact based on its height. The primary result of this theory is the plasticity index, which provides a measure of the number of asperities that are being deformed in an elastic or plastic manner. The GW theory made the following assumptions: *i*) all asperities in contact were spherical with the same radius of curvature, *ii*) asperity heights follow a Gaussian distribution, and *iii*) there is no interaction between contacting asperities. Fuller and Tabor [2] made use of the statistical framework developed by GW and used it to create an adhesive solution for JKR contact types. Their approach produced a similar adhesion index that provided a measure of the adherence force based on

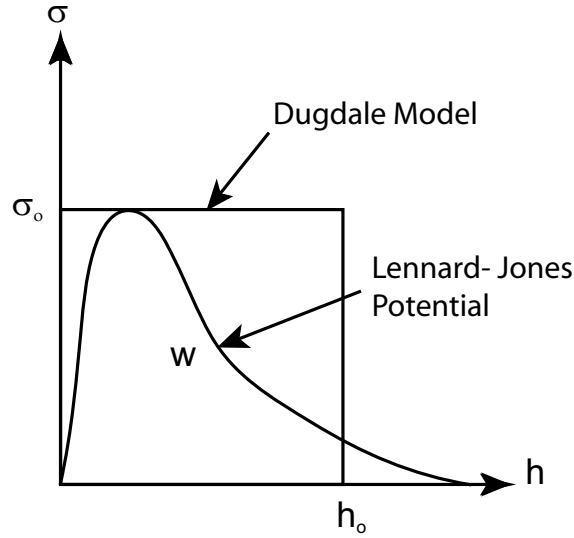


Figure 3: Dugdale and Lennard-Jones force separation laws.

JKR contact types. Maugis [14] also contributed to the adhesive rough surface contact by implementing a stochastic approach to solve for DMT contacts. His work showed that there was only a small difference in the magnitude of the adherence force when comparing the JKR and DMT rough surface solutions. However Morrow *et al* [9] extended this family of solutions by utilizing the Maugis-Dugdale solution [5] along with a modification to Maugis' theory that was provided by Kim, McMeeking, and Johnson (KMJ) [15]. The theory of KMJ added to Maugis' solution regime by considering the possibility that even though the spheres might not be in physical (intimate) contact there exists a force between them as long as they are within the range of adhesion. Morrow *et al* showed that a significant difference exists between the JKR and DMT solution regimes. By considering KMJ's extension, the overloading effect due to adhesive force was much more pronounced, thereby defining a distinct transition regime for rough surfaces.

All of the rough surface contact theories mentioned thus far are based upon conventional statistical parameters such as standard deviation of asperity heights, slope and radius of curvature. However as the ability to measure surface roughness increases to finer levels of detail, experimentalists have found that such parameters are scale dependent [16]. Just as height, slope and curvature are non-unique, the theories based on these parameters provide

scale dependent solutions as well. A need then existed for a surface characterization which was scale independent. The fractal surface characterization (see chapter 4) developed by Majumdar [17] is such a model. This model utilizes the popular Weierstrass-Mandelbrot (WM) fractal function to simulate a surface profile. Majumdar not only showed that WM could be used to simulate rough surfaces but used this model to develop a rough surface contact theory with Bhushan [18]. Their work focused on elastic-plastic contact between rough surfaces and developed expressions for the critical contact area, total area, and total load in terms of fractal dimensions. Just as GW work inspired work on adhesive rough surface contact, so too did Majumdar and Bhushan's (MB). Sahoo and Chowdhury [19] took the fractal foundation of MB theory and coupled it with the results of JKR. They developed relationships during loading and unloading conditions. Absent from their analysis, however, were expressions for total contact area and the critical area of contact. The critical area of contact refers to the limit that is reached for each individual *stretched* asperity. During unloading conditions a contacting asperity attains a critical level of stretch, after which separation abruptly occurs. These two key aspects of the analysis were provided by Morrow and Lovell [20] in a recent analysis. Sahoo and Chowdhury continued to develop theories based on their previous work [19] by developing friction and wear theories [21], [22]. It is important to note that MB fractal theory, while pioneering, lacked to note the difference between the truncated and real area of contact. The truncated area of contact is defined as the area that is created by the geometric intersection between a sphere and a flat plane. An illustrative depiction of this is shown by Figure (19) in chapter 4. This was first pointed out by Komvopoulos and Yan in [23]. Sahoo and Chowdhury used MB theory foundation without correction in their series of papers, therefore this is yet another drawback to their approximation. Morrow and Lovell make note of this discrepancy and account for the difference between the real and truncated areas. Komvopoulos and Yan contributed to adhesive theories based on a fractal characterization with [3] and [24]. In both of these works adhesive and compressive forces were uncoupled thereby bringing a degree of uncertainty into the analysis.

## 2.0 SINGLE ASPERITY CONTACT

### 2.1 ADHESIVE THEORY OF JOHNSON KENDALL, & ROBERTS (JKR)

The theory of Johnson, Kendall, and Roberts (JKR) was the first to determine the compliance relationships for the contact of elastic spheres in the presence of surface energy. The primary impetus for their work was to determine the ‘pull-off’ force between the contacting spheres. The ‘pull-off’ force is defined as the external load at which the system becomes unstable i.e. the force at which abrupt separation occurs. JKR determined this force to be:

$$F_c = -\frac{3}{2}\pi wR \quad (2.1)$$

where  $F_c$  represents the adherence for a single asperity in this case.

Johnson, Kendall and Roberts use a energy balance method to arrive at Equation (2.1). In the JKR method, the following states are assumed: *i*) a load is initially applied under a Hertzian contact condition, and at this point, the Hertzian contact load and approach are given by  $F_H$  and  $\delta_H$  respectively; *ii*) once Hertzian contact is attained, that the surface energy is then turned ‘on’ and the load is decreased while maintaining a constant contact radius. The energy balance between the two states is maintained resulting in the following equilibrium condition:

$$F_H^2 - 2F_H(F + 3w\pi R) + F^2 = 0 \quad (2.2)$$

In Equation (2.2),  $F$  is the applied load and  $F_H$  is the Hertzian contact load which is given by  $(a^3K/R)$ . By substituting  $(a^3K/R)$  for  $F_H$  this expression into Equation (2.2), the applied load is obtained:

$$F(a) = \frac{a^3K}{R} - \sqrt{6\pi w a^3 K^{1/2}} \quad (2.3)$$

where,  $a$ , is the intimate contact radius. The effective radius is given by:

$$R = \frac{R_1 R_2}{R_1 + R_2}$$

where  $R_1$  and  $R_2$  are shown in Figure (4) as the radii of each of the contacting spheres. Also recall that  $K$  is the effective modulus which combines the elastic material properties of each of the spheres by the following equation.

$$\frac{1}{K} = \frac{3}{4} \left( \frac{1 - \nu_1^2}{E_1} + \frac{1 - \nu_2^2}{E_2} \right)$$

In order to give some physical insight to the variables of this problem Figure (4) was created.

Maugis [14] alternatively expressed the equilibrium condition by developing a form of the strain energy release rate,  $\mathcal{G}$ , for this type of contact:

$$\mathcal{G} = \frac{(F_H - F)^2}{6\pi a^3 K}. \quad (2.4)$$

At equilibrium, the strain energy release rate  $\mathcal{G}$ , is equal to the work of adhesion. The stability of the system in a fixed grips configuration is the partial of  $\mathcal{G}$  with respect to the area while the approach is held constant:

$$\left( \frac{\partial \mathcal{G}}{\partial A} \right)_\delta = \frac{3K}{16\pi^2 a^3} \left( \frac{a^2}{R} - \delta \right) \left( \frac{3a^2}{R} + \delta \right) \quad (2.5)$$

where  $\delta$  is the approach distance of the contacting spheres. During rupture, or pull-off event, Equation (2.5) is less than or equal to zero. Therefore  $-3a^2/R$  represents the critical approach  $\delta$ , which can be re-written as:

$$\delta_c = - \left( \frac{3\pi^2 w^2 R}{4K^2} \right)^{1/3} \quad (2.6)$$

This expression is useful as a limit of integration when determining total load and area relationships.

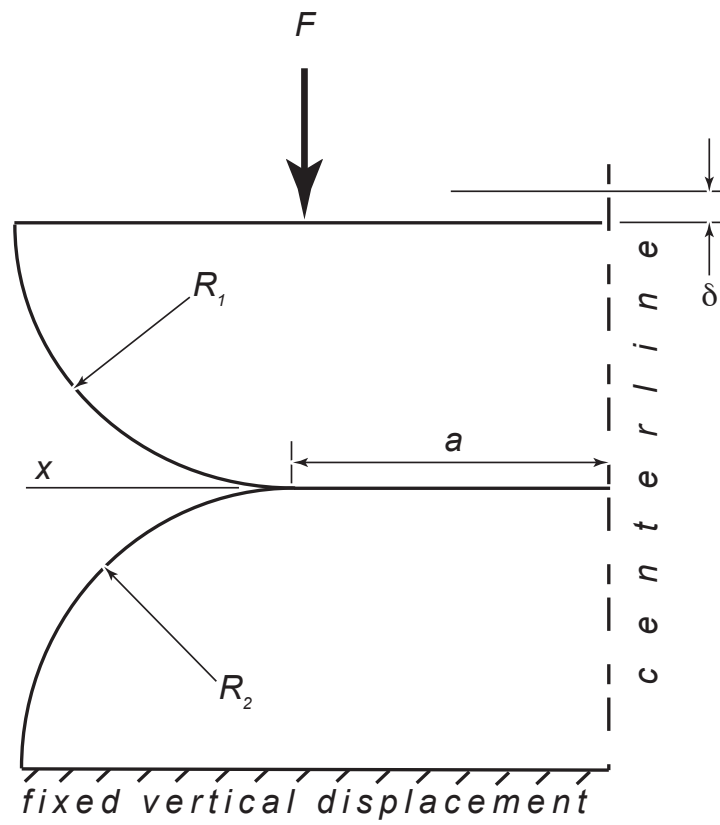


Figure 4: Depiction of physical variables used in this section.

## 2.2 JKR-DMT TRANSITION SOLUTION WITH KIM EXTENSION

Since part of this work follows the transition solution provided by Maugis, it is pertinent to review the major results of his theory. Combining the fracture mechanics solution for an axisymmetric crack subjected to a Dugdale type interior traction, with the results for the adherence of a flat punch, Maugis obtained three governing equations for the transition solution of two adhesive spheres in contact. As shown below, Equation (2.7) is a result of equilibrium between the strain energy release rate,  $\mathcal{G}$ , and the work of adhesion  $w$ . During equilibrium the stress intensity factor due to the internal loading (adhesion) cancels the stress intensity factor due to the external loading (applied load). With these two requirements the following three expressions for the dimensionless equilibrium, load, and approach are respectively given by Maugis:

$$1 = \frac{\lambda A^2}{2} [\sqrt{m^2 - 1} + (m^2 - 2) \arctan \sqrt{m^2 - 1}] + \frac{4\lambda^2 A}{3} [(\sqrt{m^2 - 1} \arctan \sqrt{m^2 - 1}) - m + 1] \quad (2.7)$$

$$\bar{F} = A^3 - \lambda A^2 \left( \sqrt{m^2 - 1} + m^2 \arctan \sqrt{m^2 - 1} \right) \quad (2.8)$$

$$\Delta = A^2 - \frac{4}{3} A \lambda \sqrt{m^2 - 1} \quad (2.9)$$

The dimensionless parameters that appear in the above equations are defined below.

$$A = \frac{a}{(\pi w R^2 / K)^{1/3}} \quad (2.10)$$

$$\bar{F} = \frac{F}{\pi w R} \quad (2.11)$$

$$\Delta = \frac{\delta}{(\pi^2 w^2 R / K^2)^{1/3}} \quad (2.12)$$

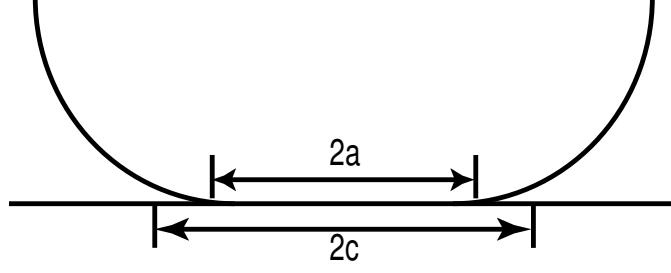


Figure 5: Intimate contact and adhesive radii.

$$\lambda = \frac{2\sigma_o}{(\pi w K^2 / R)^{1/3}} \quad (2.13)$$

where  $\delta$  is given by

$$\delta = \frac{a^2}{R} - \frac{8\sigma_o}{3K} \sqrt{c^2 - a^2} \quad (2.14)$$

In Equations (2.10, 2.14), the radius  $a$  represents the intimate area of contact and the radius  $c$  corresponds to the radius over which the adhesive traction acts (see Figure (5)). The parameter  $m$  is given by the ratio of  $c/a$ . Note that the physical depiction of  $\delta$  is clearly depicted in Figure (4). Since  $a$ ,  $F$ ,  $\delta$  represent the contact radius, the applied normal load, and the approach of the two spheres respectively, Equations (2.10 – 2.12) are their dimensionless counterparts. Kim *et al* [15] offers an extension of the Maugis-Dugdale solution by adding to the solution regime when ( $a = 0$ ) and ( $c \neq 0$ ). As Kim explains, this regime is explored by the adjustment of Equations (2.7 – 2.9):

$$\frac{\pi}{4} C^2 \lambda + \frac{2}{3} (\pi - 2) C \lambda^2 + \xi = 1 \quad (2.15)$$

$$\bar{F} = -\frac{\pi}{2} C^2 \lambda \quad (2.16)$$

$$\Delta = -\frac{4}{3} C \lambda - \frac{2}{\pi} \frac{\xi}{\lambda} \quad (2.17)$$

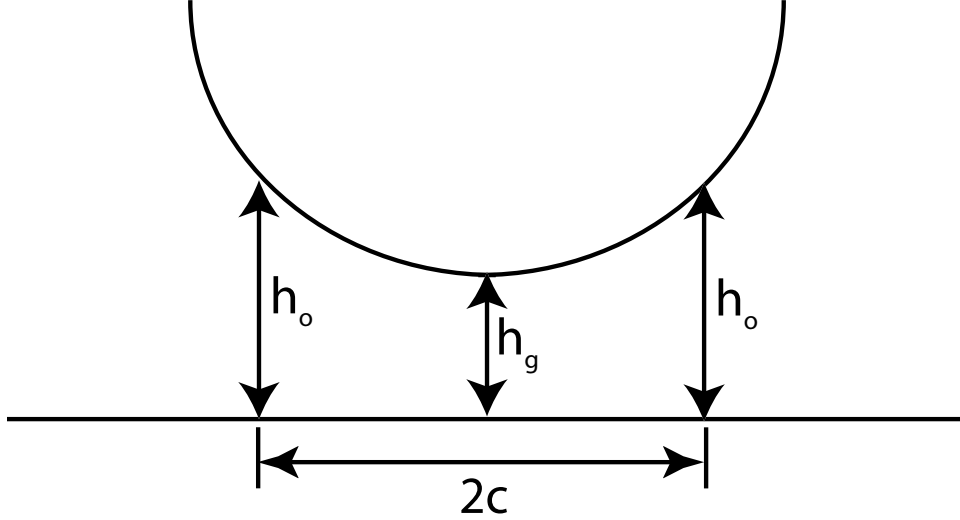


Figure 6: Representation of parameters given by Kim *et al* extension.

where  $C$  represents the dimensionless ‘adhesive contact radius’ (has a similar non-dimensional form as in Equation (2.10)) and  $\xi$  is the ratio of  $h_g/h_o$ . The parameters  $h_g$  is the gap between the deformed spheres at  $r = 0$ . Through the simultaneous solution of Equations (2.7 – 2.9) and Equations (2.15 – 2.17) figures 7 and 8 are produced. As depicted, figures 7 and 8 give a significant amount of information about the contact conditions. For example, examining the load versus deflection curve in Figure (8), two important pieces of information can be derived: (1) for each value of  $\lambda$  the horizontal tangent represents the adherence at a fixed load, and (2) the vertical tangent corresponds to separation at which abrupt pull-off occurs for fixed grips,  $\delta_c$ . The determination of  $\delta_c$  becomes an important factor when performing calculations for the rough surface with the transition solution. Now that the results of the transition solution have been presented, an approximate JKR-DMT transition solution can be generated.

### 2.3 ADHESION OF ELASTIC CYLINDERS

To compliment the adhesive elastic sphere work of Maugis, Baney and Hui [6] present an analytical solution for elastic adhesive cylinders. Their solution is analogous to the Maugis-

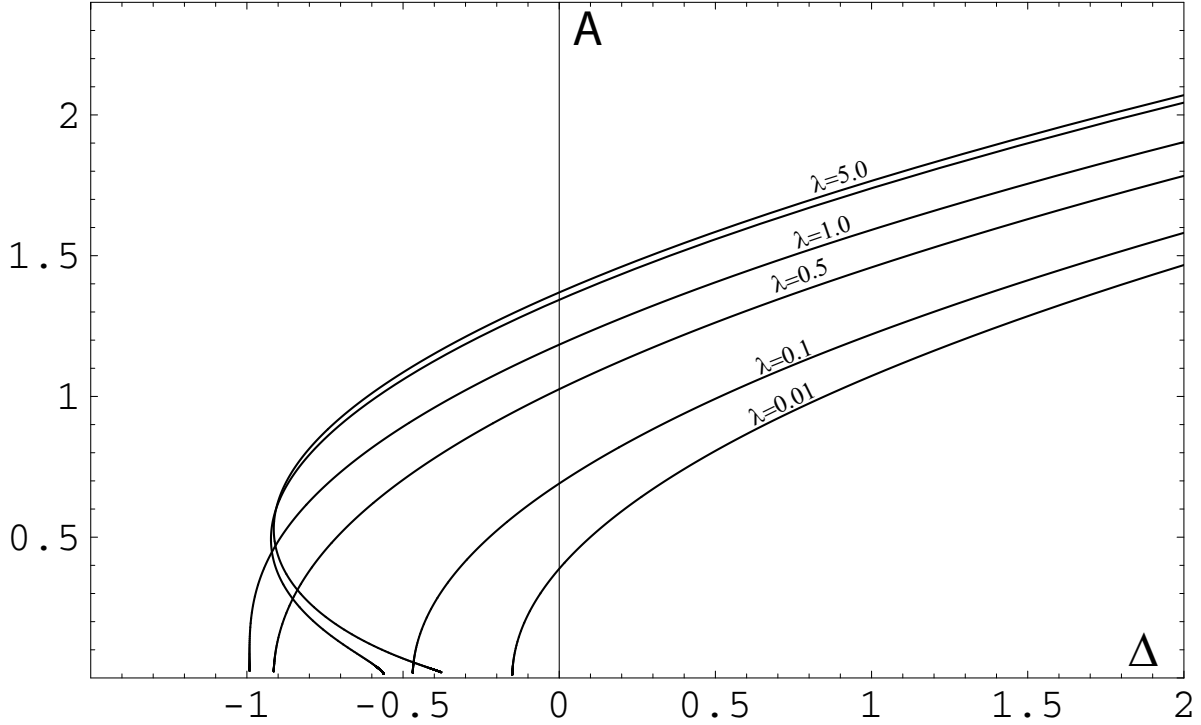


Figure 7: Variation of non-dimensional contact radius with dimensionless approach for various values of the transition parameter.

Dugdale cohesive zone type theory for the adhesion of elastic spheres outlined in Section (2.2). Baney and Hui’s theory is very useful for micro-sized contact problems that have asperities that can be modeled with a cylindrical geometry. A typical application of this theory would be adhesive contact problems in MEMS devices which have been formed by an etching process, such as micro-sized gear trains. The roughness on the surface of the MEMS gears have long cylindrical geometries. By implementing Baney and Hui’s theory into a rough surface contact model, the adherence and friction forces could be determined. Although useful in it’s present form for this purpose, the authors have neglected a portion of the solution regime by accounting for the condition when the cylinders are in direct physical contact. In this section, an extension to their solution is given which accounts for the cylinders interacting adhesively, when they are out of physical contact.

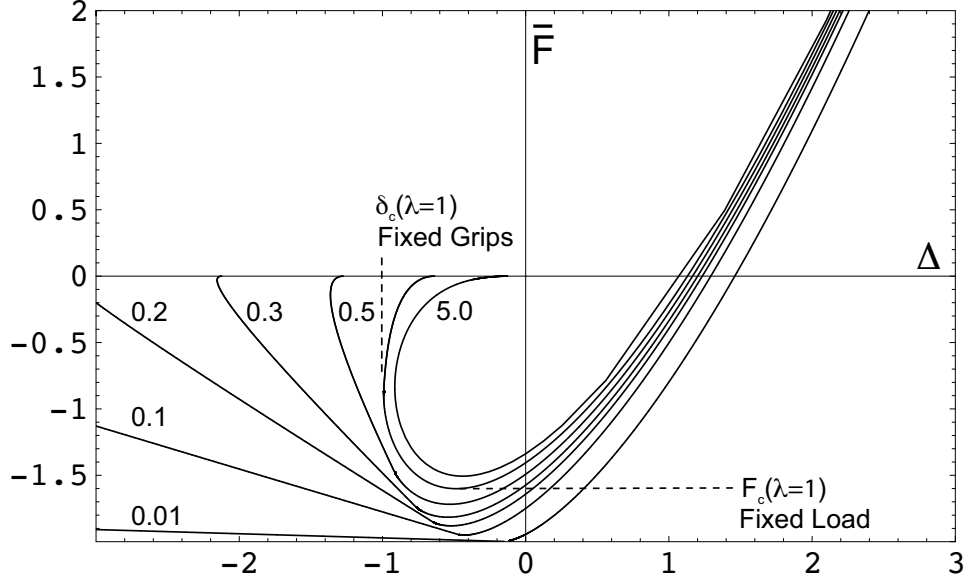


Figure 8: Dimensionless plot showing load as a function of approach for various values of the transition parameter.

### 2.3.1 BANEY AND HUI SOLUTION

Baney and Hui make use of superposition to solve the adhesive contact problem. First they compose a pressure term that satisfies the intimate contact condition, without considering surface energy. A pressure term is then composed which satisfies the adhesive forces in the cohesive zone, which does not cause displacements inside the intimate contact region.

The geometry of this adhesive contact problem of cylinders is shown in Figure (9). This figure shows the location of the cohesive zone that acts until the air gap between the deformed spheres becomes greater than the separation of  $h_o$ . The magnitude of the adhesive traction is constant,  $\sigma_o$ , that acts from the point of intimate contact till the air gap becomes greater than  $h_o$ . This cohesive zone extends along the entire length of the cylinder. The contact condition is given by:

$$w_1(x) + w_2(x) = -\frac{x^2}{2R} \quad (2.18)$$

where the functions  $w_1(x)$  and  $w_2(x)$  describe the displacement of each point of the cylinders profile along the  $x$  axis. The effective radius is given by:

$$R = \frac{R_1 R_2}{R_1 + R_2}$$

where  $R_1$  and  $R_2$  are shown in Figure (9) as the radii of each of the contacting cylinders. Figure (10) physically depicts the intimate contact region  $|x| \leq a$  as  $x = \pm a$  and the adhesive radius which is defined by the region between  $x = \pm b$ , where  $b > a$ . Their model considers the cohesive zone similar to Maugis [5] with a Dugdale model Figure (3). The pressure term which satisfies the contact without considering adhesion,  $p_c$ , is given by:

$$p_c(x) = \frac{3K}{8R}(a^2 - x^2)^{1/2} + p'_o(a^2 - x^2)^{-1/2} \quad (2.19)$$

Note the pressure term in  $p_c$  which involves  $p'_o$  creates a singularity condition at the edge of the intimate contact area. It should be noted that this term  $p'_o$  would normally be neglected, positive values it would infer that interference existed outside the contact area and negative values would only be valid in the case of adhesive forces. Since the adhesive forces are taken into account in this problem the  $p'_o$  term cannot be set to zero. For the case where the cohesive zone interaction is considered the pressure term becomes

$$p_d(x) = \begin{cases} \frac{2\sigma_o}{\pi} \left[ \sqrt{\frac{b^2 - a^2}{a^2 - x^2}} - \tan^{-1} \sqrt{\frac{b^2 - a^2}{a^2 - x^2}} \right] & : |x| \leq a \\ -\sigma_o & : a < |x| < b \end{cases} \quad (2.20)$$

where  $p_d$  denotes the ‘Dugdale pressure’. The Barenblatt condition is then invoked which states that the singularities in pressure from the contact and cohesive zone must cancel one another. Thus  $p'_o$  is required to be

$$p'_o = -\frac{2\sigma_o}{\pi} \sqrt{b^2 - a^2}.$$

To illustrate where these pressure terms,  $p_c$ ,  $p_d$ , and  $p$  act Figure (10) was created. This leaves the pressure in the contact zone,  $|x| < a$ , to be

$$p(x) = \frac{3K}{8R}(a^2 - x^2)^{1/2} - \frac{2\sigma_o}{\pi} \tan^{-1} \sqrt{\frac{b^2 - a^2}{a^2 - x^2}} \quad (2.21)$$

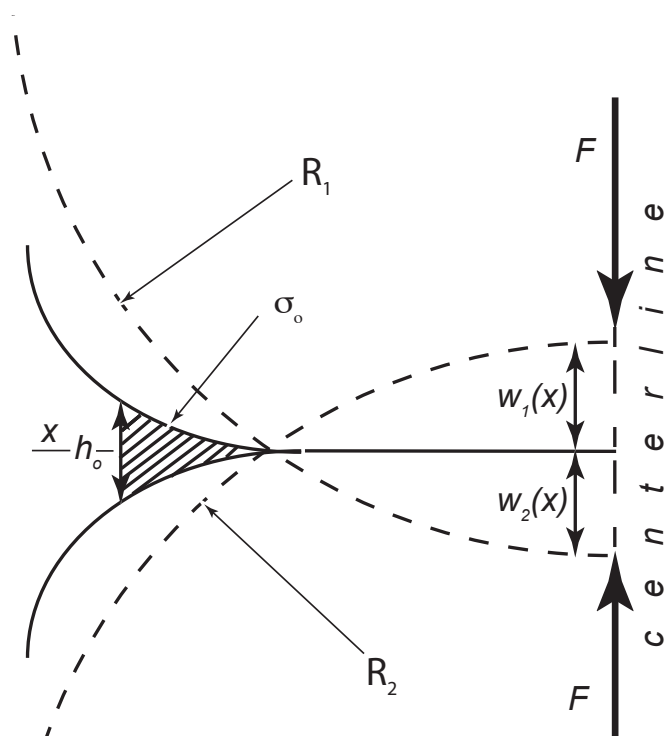


Figure 9: Geometry of the cylinders in contact.

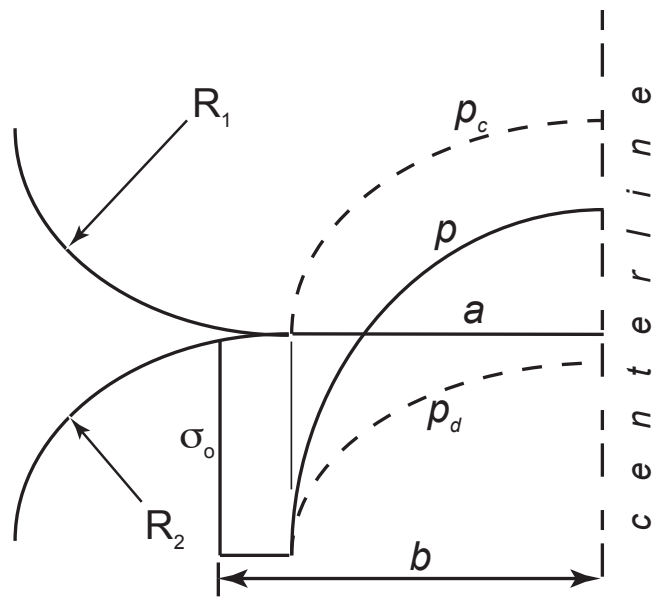


Figure 10: Physical description of pressure distributions.

The pressure is then integrated over the contact and cohesive zones which gives the total force.

$$F = \frac{\pi K}{3R} a^2 - 2\sigma_o \sqrt{b^2 - a^2} \quad (2.22)$$

Baney and Hui finally find the critical opening gap at  $x = b$ ,

$$h_o = \frac{b\sqrt{b^2 - a^2}}{2R} - \frac{a^2}{2R} \ln \frac{b + \sqrt{b^2 - a^2}}{a} - \frac{3\sigma_o}{\pi K} b \ln \frac{b}{a} + \frac{3\sigma_o \sqrt{b^2 - a^2}}{\pi K} \ln \frac{b + \sqrt{b^2 - a^2}}{a} \quad (2.23)$$

### 2.3.2 ANALYTICAL EXTENTION TO BANEY-HUI SOLUTION

In an attempt to generalize the above derived expressions Baney *et al* introduce the following non-dimensionalization for the variables in equations (2.22-2.23):

$$\tilde{F} = \frac{F}{(\pi(3/4)Kw^2R)^{1/3}} \quad (2.24)$$

$$\tilde{a} = \frac{a}{2 \left( \frac{R^2 w}{\pi(3/4)K} \right)^{1/3}} \quad (2.25)$$

$$\tilde{B} = \frac{b}{2 \left( \frac{R^2 w}{\pi(3/4)K} \right)^{1/3}} \quad (2.26)$$

$$\lambda = \frac{4\sigma_o}{\left( \frac{\pi^2((3/4)K)^2 w}{R} \right)^{1/3}} \quad (2.27)$$

$$\xi = \frac{a}{b} \quad (2.28)$$

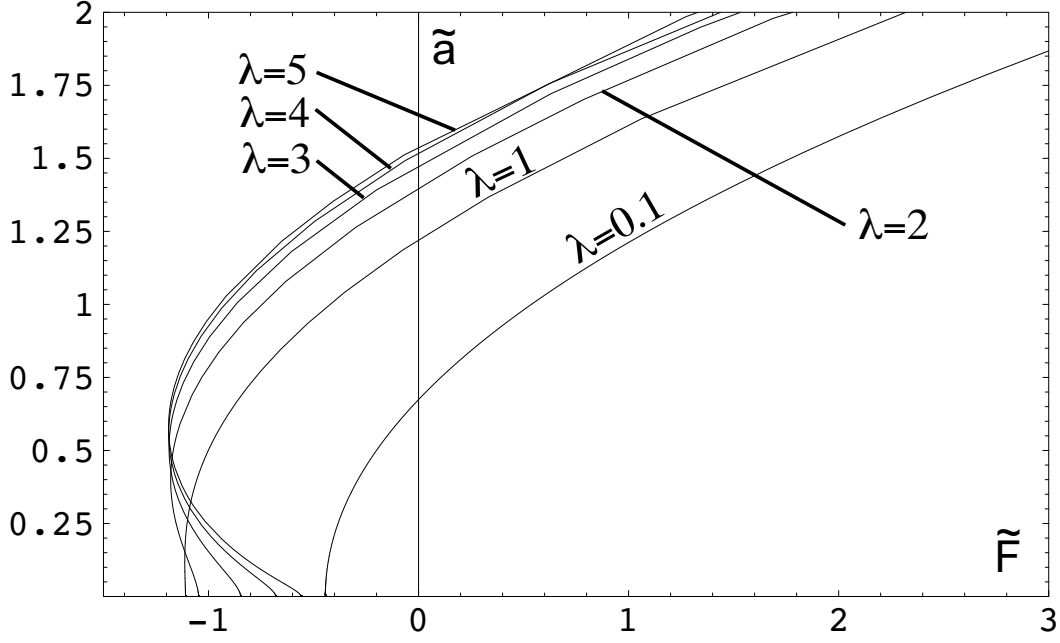


Figure 11: Intimate contact radius versus load.

where  $F$ ,  $a$ ,  $b$ ,  $\lambda$ , and  $\xi$  are the load, contact radius, adhesive contact radius, transition parameter, and intimate to adhesive contact radius ratio respectively. By utilizing the dimensionless parameters and the condition that  $w = \sigma_o h_o$ , Equations (2.22, 2.23) can be written as:

$$\tilde{F} = \tilde{B}^2 \xi^2 - \tilde{B} \lambda \sqrt{1 - \xi^2} \quad (2.29)$$

$$1 = \frac{\tilde{B}^2 \lambda}{2} \left[ \sqrt{1 - \xi^2} - \xi^2 (\ln(1 + \sqrt{1 - \xi^2}) - \ln(\xi)) \right] + \frac{\tilde{B} \lambda^2}{2} \left[ \ln(\xi) + \sqrt{1 - \xi^2} (\ln(1 + \sqrt{1 - \xi^2}) - \ln(\xi)) \right] \quad (2.30)$$

when  $\tilde{a} \neq 0$ , that is the cylinders are in physical contact. Note Equation (2.30) is a bit more difficult to attain than Equation (2.29). First the Equation (2.23) must be divided through by  $h_o$  and  $w = \sigma_o h_o$  is used to eliminate  $h_o$  from the equation. Then the non-dimensional parameters are used to re-write the equation in the final form given by Equation (2.30).

One contribution of the present work is to extend this solution to include the regime to when the cylinders are no longer in physical contact but they remain within the range of adhesion. The solution for this region is given by the following equations.

$$\tilde{F} = -\lambda\tilde{B} \quad (2.31)$$

$$1 = \frac{\tilde{B}^2\lambda}{2} + \frac{\tilde{B}\lambda^2}{2}\ln(2) + \delta \quad (2.32)$$

where  $\delta = h_g/h_o$ . The parameter  $\delta$  is comprised of  $h_g$  and  $h_o$ , which are physically depicted in Figure (6). In Equation (2.23) the value for  $h_g = 0$ , therefore when the equation was non-dimensionalized,  $\delta$  did not appear. It should be noted that  $\delta$  in this sub-section now refers to this ratio and does not relate to the approach distance of the cylinders. Since we now want are considering a physical separation between the two cylinders the  $\delta$  does appear if  $h_g$  is used to represent the separation of the cylinders at the point of closest approach. From the figure, it is found  $\delta$  represents the ratio of the gap at  $r = 0$  to the critical opening gap,  $h_o$ . These are adjustments to Equations (2.29, 2.30) by letting  $a$  tend to zero and accounting for  $\delta$  in Equation (2.32). Using these newly derived expressions, Figure (12) can be produced. It is interesting to note in Figure (12) that in the solution regime where there is no physical contact, the load varies nearly linearly with the adhesive contact radius. Equations (2.31, 2.32) and Figure (12) complete the cohesive zone model for cylinders. Now this asperity model can now be implemented into rough surface theories to solve for adhesion on the micro-scale.

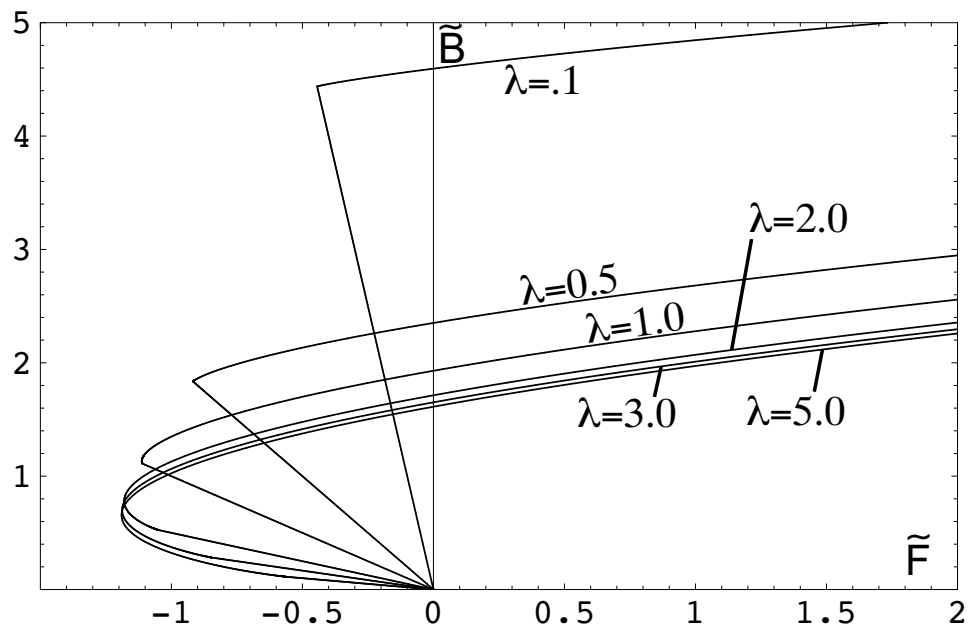


Figure 12: Adhesive contact radius versus load.

## 3.0 G-W TYPE TRANSITION SOLUTION FOR ROUGH SURFACES

### 3.1 INTRODUCTION

In this chapter a method of approximating the pull-off or adherence force is presented in the case for which the dominant length scale of surface roughness is known *a priori*. Although engineering surfaces have been shown to exhibit roughness on several different length scales [17], different types of surface machining and grinding methods can restrict the range of length scales [25]. For example, if a surface is being prepared by a cutting tool that has a known radius of curvature one would expect that the surface to exhibit fractal behavior at length scales less than or equal to the radius of the cutting tool. However, when the examining the surface at a scale larger than the radius of the cutting tool, the surface topography becomes deterministic. Later chapters will explore the fractal surface roughness regime, however, this chapter is presented to give an adhesive solution for surfaces where the length scale is known but the adhesive contact type is not. A rough surface solution of adhesive contact is given for the transition regime which exists between the JKR and DMT solutions.

### 3.2 BACKGROUND

Maugis [14] used an approach similar to Fuller and Tabor's to arrive at a solution for contacts of the DMT type. In order to bridge the gap between Fuller and Tabor's solution and the one presented by Maugis [14], this chapter focuses on the development of an adhesive solution for rough surfaces utilizing Maugis' JKR-DMT transition solution. It is important to note

Table 3: Single asperity and Rough Surface adhesive theories

Geometry	Theory	Solution Regime
Elastic Spheres	JKR	$\lambda = \infty$
	Maugis-Dugdale	Small to large $\lambda$
	DMT	$\lambda = 0$
Adhesive rough surface	Fuller & Tabor (JKR)	$\lambda = \infty$
	<i>Present chapter (Maugis-Dugdale)</i>	Small to large $\lambda$
	Maugis' (DMT)	$\lambda = 0$

that K.S. Kim *et al* [15] offered an extension of Maugis' solution for the case when the two spheres are not in intimate contact but within the range of adhesion. Kim *et al* theory should now be considered an integral part of the Maugis model; therefore it will be included when Maugis' transition theory [5] is referenced in this chapter. Table 3 explains the applicability of Maugis transition solution for single asperities and demonstrates how the current chapter will similarly complete the theories for adhesive rough surface contact.

### 3.3 APPROXIMATION OF MAUGIS' TRANSITION SOLUTION

A drawback of equations Equations (2.7 – 2.9) and Equations (2.15 – 2.17) is that they are cumbersome to manipulate in order to attain meaningful results. To use these equations in a more efficient manner, figures 7 and 8 were numerically curve fit using a non-linear regression program. Expressions for  $\bar{F}$  and  $A$  were then determined as functions of  $\Delta$ . Recall the non-dimensional parameters from the JKR-DMT transition theory of Maugis presented in Section (2.2).

$$A = \frac{a}{(\pi w R^2 / K)^{1/3}}$$

$$\bar{F} = \frac{F}{\pi w R}$$

$$\Delta = \frac{\delta}{(\pi^2 w^2 R / K^2)^{1/3}}$$

$$\lambda = \frac{2\sigma_o}{(\pi w K^2 / R)^{1/3}}$$

These are shown here once again because they are readily used throughout the remainder of this chapter. A physical illustration of these parameters is given in Figure (4) in chapter 2. Once these expressions were obtained, they were substituted into integrals resulting from the rough surface analysis (c.f. Greenwood [13] and Fuller, Tabor [2]) to produce approximations of the pull-off force and contact area for varying approach distances. It should be noted that these equilibrium curves  $\bar{F}(\Delta)$  and  $A(\Delta)$  were only fit within the stable region of Maugis' solution.

For values of  $\lambda \geq 1$ , the contact radius and load deflection curves were fit in a two stage process. First, the dimensionless contact radius  $A$  was fit with respect to the dimensionless deflection parameter  $\Delta$  into the following:

$$\bar{F} = \alpha + \beta A^\theta + \gamma A^\omega \quad (3.1)$$

where  $(\alpha, \beta, \gamma, \theta, \text{ and } \omega)$  are curve fit constants. From Equation (3.1), the load deflection curve was produced. The motivation for the form is found in equation Equation (2.8), where an expression for the contact radius versus deformation becomes directly available. The dimensionless contact radius parameter,  $A$ , was likewise fit in a similar manner using the form derived from Equation (2.9). This form is given by:

$$A = \eta + (\rho + \theta \Delta)^\varphi. \quad (3.2)$$

where  $\eta, \rho, \theta, \varphi$  are curve-fit constants.

When  $\lambda < 1$ , fitting the Maugis and Kim region was more challenging. After investigating many different function forms the following expression was found to be optimum.

$$\begin{aligned} \bar{F} = & y_o + A^* [\exp(-0.5(\Delta - xc1)^2/w) \\ & + B(1 - \tanh(k_2(\Delta - xc2))) \exp(0.5k_3(|\Delta - xc3| + (\Delta - xc3)))] \end{aligned} \quad (3.3)$$

where  $y_o, A^*, xc1, w, B, k_2, xc2, k_3$  and  $xc3$  are all parameters. An example of the quality of fits is shown for  $\lambda = 0.2, 0.5, 0.9, 5.0$  in Figure (13). The curve-fits for all  $\lambda$  investigated

Table 4: Values for curve-fit parameters for transition parameter values less than one (see Appendix A for values greater than one).

$\lambda$	$y_o$	$A^*$	$xc1$	$w$	$B$	$k_2$	$xc2$	$k_3$	$xc3$
0.2	122.253	-122.684	-1.741	251.731	0.025	0.674	-0.792	0.304	-0.545
0.3	16.005	-17.329	-0.547	17.158	0.041	2.020	-0.872	0.783	-0.721
0.5	10.441	-9.910	-0.230	9.080	0.258	2.010	-1.415	0.253	-0.855
0.9	11.368	-7.566	0.702	6.681	0.967	1.580	-1.570	0.300	-0.942

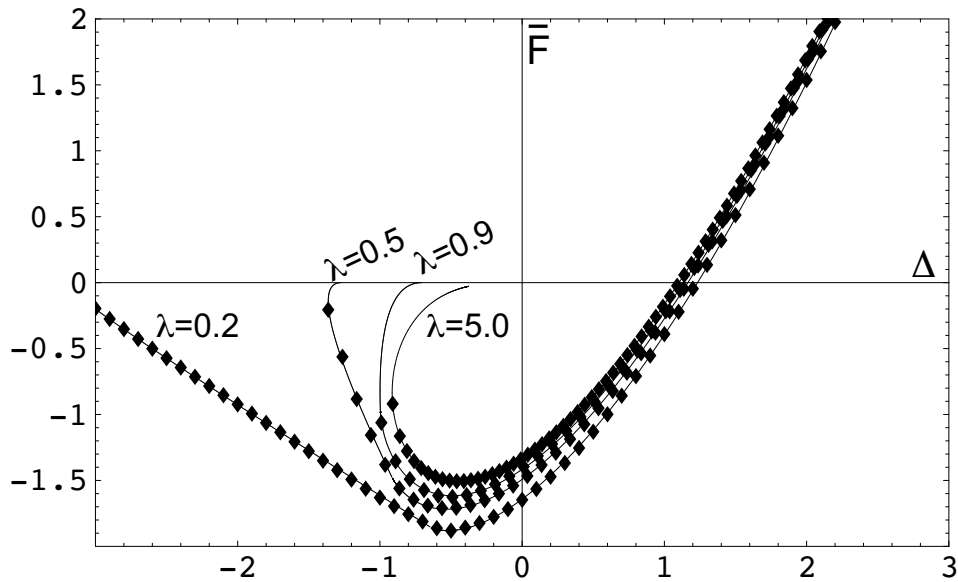


Figure 13: The black curves represent the solution given from Maugis' solution, and in white the curve-fit results are shown laid overtop.

in this are listed in Appendix A. With the approximate equations for  $\bar{F}$  and  $A$ , the rough surface analysis of Fuller and Tabor can be implemented.

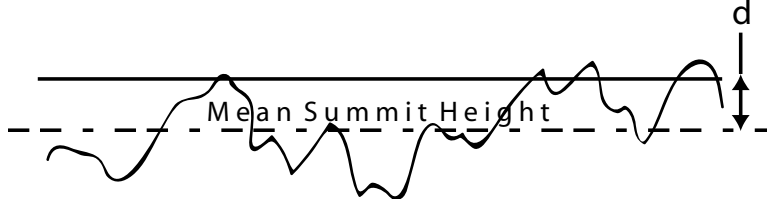


Figure 14: Depiction of composite rough surface at a separation of  $d$ .

### 3.4 METHODOLOGY FOR ADHESIVE ROUGH SOLUTION

It can be assumed that two rough surfaces being brought into normal contact, with standard deviations in asperity heights of  $\sigma_1$  and  $\sigma_2$ , can be replaced with a single surface of roughness  $\sigma = \sqrt{\sigma_1^2 + \sigma_2^2}$  and a smooth surface. This method of replacing the rough surface interface by a smooth rigid plane and a deformable rough surface of  $\sigma$  is taken to be common practice throughout literature [2], [5], [13], [26]. However strong physical evidence has not been demonstrated that this *truly* represents the roughness of the interface. If it is assumed that there exists a probability density function  $\varphi(z)$  of asperity heights, then it is possible to find the probability that an asperity will be greater than a certain height,  $d$ . The distance  $d$  represents the length from the mean plane of asperity heights to the smooth surface (Figure (14)). The probability that an asperity height is greater than  $d$  is given by:

$$\int_d^{\infty} \varphi(z) dz. \quad (3.4)$$

Therefore it follows that the number of asperities in contact is represented by:

$$n = N \int_d^{\infty} \varphi(z) dz \quad (3.5)$$

where  $N$  represents the total number of asperities. Having the numerical expressions for the non-dimensional contact radius ( $A$ ) and load ( $\bar{F}$ ) for a single asperity as a function of  $\Delta$ , the following integrals can be formed.

$$S_{total} = N(\pi w R^2 / K)^{2/3} \int_d^{\infty} \pi A(\Delta)^2 \varphi(z) dz \quad (3.6)$$

$$F_{total} = N\pi w R \int_d^{\infty} \bar{F}(\Delta) \varphi(z) dz \quad (3.7)$$

Equation (3.6) and Equation (3.7) represent estimates of the total contact area and load. Note that all of the above integrals are carried out in terms of  $z$ . Since the expressions for the load and contact area are in terms of  $\Delta$ , it is necessary to have a relationship between  $\Delta$  and  $z$ . The asperities that have a height greater than  $d$  are deformed by a distance  $\delta = z - d$ . Recalling the definition of  $\Delta$  in Equation (2.12), and assuming a Gaussian distribution:

$$\varphi(z) = \frac{1}{\sigma\sqrt{2\pi}} \exp\left(\frac{-z^2}{2\sigma^2}\right) \quad (3.8)$$

Variable  $z$  is changed to  $\delta$  in Equation (3.7) and the following equation is obtained:

$$\frac{F_{total}}{N\pi w R F_c(\lambda)} = \frac{1}{\sigma F_c(\lambda)\sqrt{2\pi}} \int_0^\infty \bar{F}\left(\frac{\delta}{\bar{\delta}}\right) \exp\left(-\frac{(\delta + d)^2}{2\sigma^2}\right) d\delta \quad (3.9)$$

where  $\bar{\delta}$  is  $(\pi^2 w^2 R / K^2)^{1/3}$ . Note see Figure (8) for a depiction of  $F_c$  as a function of  $\lambda$ . As explained in [2], however, Equation (3.9) is only valid when the smooth surface progressively approaches the rough surface until a minimum  $d$  is reached. Consider the case when after minimum separation distance  $d$  is reached that the surfaces are then subsequently separated. During this separation, Equation (3.9) will no longer be valid because the asperities that were extended above their  $\delta_c$  will no longer contribute to the adherence force. An interesting way to show the effect of asperities which are stretched is to examine the Gaussian distribution of asperities heights. The asperities which are physically interfering with the rigid plane have a height greater than  $d$ . These are shown in Figure (15) by the gray shaded area with  $z$  greater than  $d$ . Whereas the stretched asperities are range from  $d - \delta_c$  to  $d$  that are depicted by the black shaded region. Therefore in order to improve Equation (3.9), so that the adherence force can be ascertained, the lower limit of integration needs to be corrected by the amount  $\delta_c(\lambda)$  which is represented in Figure (8). After making the adjustment to the lower integration limit and eliminating  $\sigma$ , Equation (3.9) takes the following form.

$$\frac{F_{total}}{N\pi w R F_c(\lambda)} = \frac{1}{F_c(\lambda)\sqrt{2\pi}} \int_{-\delta_c^*(\lambda)}^\infty \bar{F}\left(\frac{\delta^*}{\bar{\delta}^*}\right) \exp\left(-\frac{(\delta^* + d^*)^2}{2}\right) d\delta^* \quad (3.10)$$

Any term in Equation (3.10) that has a superscript  $*$  has been divided by  $\sigma$ . Equation (3.10) is similar in form to Fuller and Tabor's rough surface integral, however there is some important difference that should be noted. The lower integration limit  $\delta_c$ , and  $F_c$  are functions of  $\lambda$ , which gives the solution validity over the range of the transition parameter, whereas

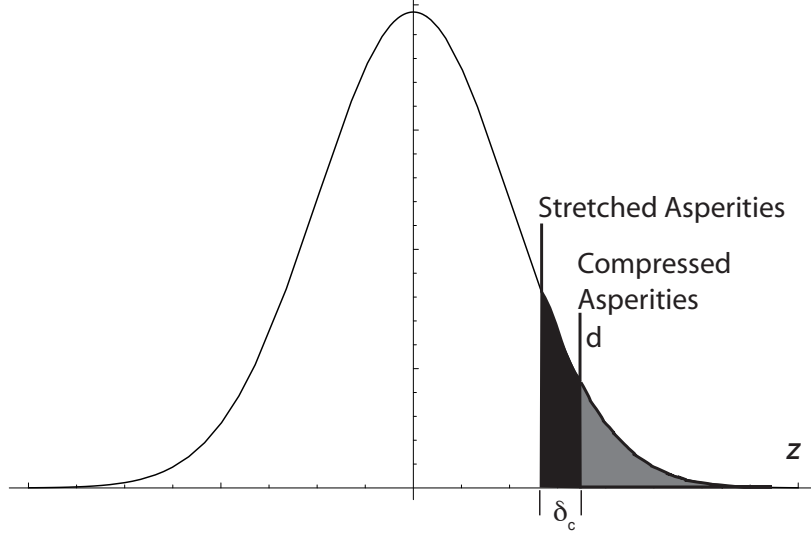


Figure 15: Probability of an asperity being stretched or compressed.

in [2] the integral is only valid for the regime of JKR. For Equation (3.10) values for  $F_c(\lambda)$  and  $\delta(c)$  need to be determined. The normalization factor  $F_c(\lambda)$  is determined by finding the point at which the tangent for the load deflection curve becomes zero. It is at this location that the pull-off force is found for a single asperity. In a similar manner,  $\delta_c(\lambda)$  can be determined. For  $\delta_c$ , however, the point at which the tangent becomes vertical is taken, which yields the amount of stretching that an asperity can take under a fixed grip condition. A similar integral is obtained for the total contact area and is given by Equation (3.11)

$$\frac{A_{total}}{N(\pi w R^2 / K)^{2/3} A_c(\lambda)} = \frac{\pi}{A_c(\lambda) \sqrt{2\pi}} \int_{-\delta_c^*(\lambda)}^{\infty} A \left( \frac{\delta^*}{\bar{\delta}^*} \right)^2 \exp \left( -\frac{(\delta^* + d^*)^2}{2} \right) d\delta^* \quad (3.11)$$

The critical step in obtaining an adhesive rough surface solution is to find the load at which the system becomes unstable, i.e. the minimum pull-off force ( $F_{min}$ ). In order to find the magnitude and the value of  $d^*$  for this critical load, the derivative of Equation (3.10) must be taken and set equal to zero. Then  $d^*$  is solved for and the value of the pull-off force is computed. As Maugis shows in [14], the derivative can be taken within the integral sign and

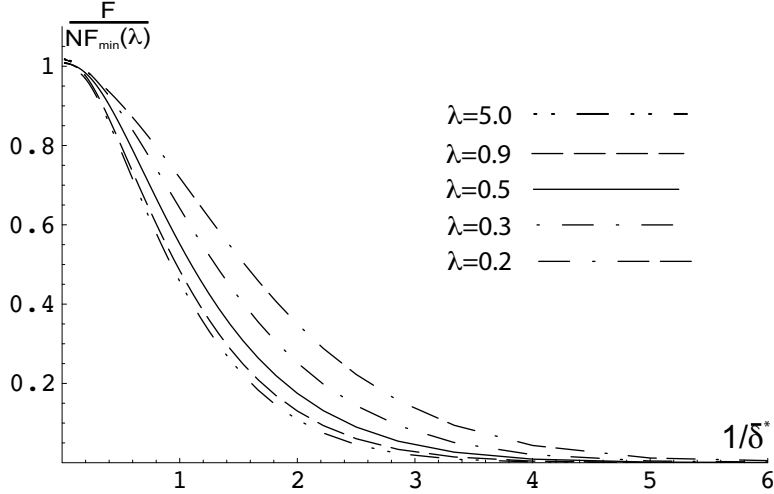


Figure 16: Adherence force for rough surfaces for various values of the transition parameter.

the derivative can be taken with respect to  $d^*$ . In taking the derivative of Equation (3.10) the following expression is obtained:

$$\int_{-\delta_c^*(\lambda)}^{\infty} \bar{F} \left( \frac{\delta^*}{\bar{\delta}^*} \right) (d^* + \delta^*) \exp \left( -\frac{(\delta^* + d^*)^2}{2} \right) d\delta^* = 0. \quad (3.12)$$

Equation (3.12) allows to solve for  $F_{min}$  as a function of  $\lambda$ .

### 3.5 RESULTS

Equation (3.12) was utilized to study the effect that varying  $\lambda$  had on the adherence force. The results of these calculations are depicted in Figure (16), where results are shown out to a value of  $\lambda = 0.2$  because of the difficulty that arises when approximating the load deflection curve.

Closely examining Figure (16), several interesting trends are found. The first trend shows that the rate of decay of the adherence force distinctly varies with the value of  $\lambda$ . For larger values (5.0) of  $\lambda$  in the JKR range, the adherence force rapidly decreases as a function of  $1/\bar{\delta}^*$ . As  $\lambda$  decreases and tends toward the DMT regime, however, the rate of change of the adherence force substantially decreases. Such a difference in the decay rates can be directly

attributed to the fact that the harder, less compliant DMT materials have a significantly greater adhesion range than the more compliant JKR materials.

A second important tendency found in Figure (16) is that the separation behavior of JKR materials are dramatically different than DMT materials. As the value of  $\lambda$  is decreased the normalized adherence force increases for any one value of  $1/\bar{\delta}^*$ . This phenomenon is referred by Maugis in [8] as overloading due to adhesion. This analysis not only accounts ‘adhesive ring’ outside of the stretched asperities but also incorporates the attractive force of the asperities that are no longer in intimate contact but are within the range of strong interaction,  $h_o$ . This effect is directly attributed to the inclusion of Kim *et al* extension of Maugis’ theory.

Finally, in Figure (16), it appears that the DMT regime will have a greater separation force than those of JKR materials. This phenomenon, however, is an artifact of the use of identical material parameters for JKR and DMT materials when generating the curves in Figure (16). In reality, DMT materials have significantly larger elastic properties (i.e. Young’s modulus) than JKR materials. Therefore, being much more compliant and having a higher peak traction than their DMT counterparts, the elastic energy of compressed asperities in JKR materials will naturally generate greater peak adhesive forces than DMT materials.

The adherence force is plotted versus the adhesion parameter,  $1/\bar{\delta}^*$ . This adhesion parameter is essentially the same as that used by Fuller and Tabor, in fact, the difference is a scaling factor. An identical adhesional parameter was specifically used to demonstrate the effect of adherence force with the variation of  $\lambda$  which could easily be compared to the results of Fuller and Tabor. The adhesion parameter of Fuller and Tabor is sufficient because it offers a measure of the competing elastic and adhesional forces.

### 3.6 SUMMARY AND DISCUSSION

Within the statistical frame work laid out by Greenwood and Williamson, the adherence force has been predicted for various values of the transition parameter  $\lambda$  by using an approximation for Maugis’ solution. This theory is only valid for surfaces that have been compressed to a certain distance and then separated. Unlike the theory of Fuller and Tabor [2], and solution

of Maugis [8] this chapter accounts for the adhesive forces due to asperities which are no longer in physical contact but are within the adhesive range of neighboring surfaces.

Now that the normal force between the two solids has been determined, further studies can utilize this information in relation to frictional forces between rough surfaces as  $\lambda$  is changed. As Maugis mentions in [8], the overload due to adhesion can increase frictional forces. Since his solution for contacts of the DMT type does not account for asperities that are within the adhesive range however are not in physical contact his estimation of the adherence force may be lower than predicted in this chapter.

## 4.0 FRACTAL MODEL FOR ADHESIVE CONTACT OF JKR TYPE

### 4.1 INTRODUCTION

In chapter 3 an assumption was made which restricts the applicability of the derived expressions to a certain length scale. This statistically based theory can be used with confidence as long as the length scale is known before hand. In this present chapter, it is assumed that the surface interface exhibits fractal behavior. This means that the surface has roughness on several different length scales and the contact type is governed by the adhesive contact of Johnson, Kendall and Roberts [4].

### 4.2 BACKGROUND

Based on a single asperity solution provided by Johnson, Kendall and Roberts [4] (JKR), an adhesive rough surface model will be developed in this chapter using a fractal surface characterization. Similar to the fractal counterpart of the G-W model presented by Majumdar and Bhushan [18], the current work employs a unique scale independent fractal model that complements the solution obtained by Fuller and Tabor [2] (see Table 5).

Table 5: Rough surface contact theories.

	Conventional Statistical	Fractal Model
Elastic-Plastic	Greenwood & Williamson [13]	Majumdar & Bhushan [18]
Elastic Adhesive (JKR)	Fuller & Tabor [2]	<i>Present chapter</i>

In a work with a similar premise to the present chapter, Sahoo and Chowdhury [19] analyzed the adhesive contact between rough surfaces using a modified JKR approach. In their analysis, Sahoo and Chowdhury included plasticity of asperities and based their analysis on the truncated area of contact. Unlike the work presented in [19], the authors have assumed that plasticity plays a minor role in the asperity contact due to the light loading conditions. Furthermore, Sahoo and Chowdhury fail to denote the difference between the real and apparent area of contact, whereas the present work makes this distinction and provides a means of conversion between truncated and JKR contact areas (this is discussed in detail in Section (4.4)).

It is also important to note that two and three-dimensional comparisons of uncoupled compressive and adhesive force contributions have been previously determined for a given separation distance [3],[24]. A unique feature of the present JKR based model, however, is that the forces are computed by directly coupling the elastic deformation and adhesive effects. Such an approach more effectively captures the physical phenomenon being analyzed. In addition to improving accuracy, this coupled model is potentially very useful for MEMS designers because it allows determination of adhesive forces as a direct function of easily obtainable fractal ( $G$  and  $D$ ) and material parameters.

### 4.3 FRACTAL SURFACE CHARACTERIZATION

As mentioned in Section (1.3), conventional statistical methods of surface characterization are scale dependent. Therefore any contact theory that is based on a statistical description is subject to errors [2] or [13]. It is well documented that surfaces exhibit roughness on many different length scales [16], [17], [18], and [27]. The topography of any surface can be thought of as roughness superimposed on top of roughness. In a series of papers by Majumdar *et al* [16] and [28], it has been shown that the multi-scale nature for surface roughness can be represented by fractal geometry.

For the present analysis, the surface profile height is represented by  $z(x)$ , which is defined by the real part of the Weierstrass-Mandelbrot function:

$$z(x) = G^{(D-1)} \sum_{n=n_l}^{\infty} \frac{\cos(2\pi\eta^n x)}{\eta^{(2-D)n}} \quad 1 < D < 2 \quad \eta > 1. \quad (4.1)$$

In Equation (4.1),  $D$  is the fractal dimension,  $G$  is a scaling constant (which carries a length unit), and  $n_l$  is defined by the lowest frequency of observation that corresponds to the length of the sample,  $L$ ,  $\eta^{n_l} = 1/L$ . Adjustments have been made by Majumdar and Bhushan [16] to the original W-M function introduced by Berry and Lewis [29]. These include starting the summation at  $n_l$  and multiplying the function by the scaling relation  $G^{D-1}$ . Majumdar and Tien [28] found that  $\eta = 1.5$  is a suitable value for phase randomization. Setting  $\eta = 1.5$  then provides a means of solution for  $n_l$  assuming the length of the sample is known.

In order to determine the fractal parameters  $D$  and  $G$ , the power spectrum of  $z(x)$  is utilized. The power spectrum of  $z(x)$  is found by taking its Fourier transform. Berry and Lewis showed the power spectrum can be approximated by taking the average range of  $\Delta\omega$  and  $\Delta n$  such that the power spectrum becomes:

$$P(\omega) = \frac{G^{2(D-1)}}{2\ln\eta} \frac{1}{\omega^{(5-2D)}} \quad (4.2)$$

The parameters  $G$  and  $D$  are then found by plotting the power spectrum of the fractal surface, where  $D$  is the slope and  $G$  is found from the intersection of the vertical axis. This solution assumes that the roughness of the contact interface is exhibited on several different length scales. By plotting the power spectrum density, one can determine the finite range of length scales for which the surface is fractal. At the spatial frequency which the surface deviates from the power-law behavior the limits are determined. Experimental data from atomic force microscope scans are presented in chapter 5 to illustrate this phenomenon. The power spectrum density of this equivalent rough surface interface is shown in Figure (17) to illustrate the range of length scales for which the interface exhibits fractal behavior. It is seen in Figure (17) that for lower frequency values the roughness of the interface is tending away from a fractal trend. This is an artifact of the surface scans which were chosen. In chapter 5 the roughness profiles which form the interface are shown. One of these surfaces has dominant ribs which were intentionally manufactured to reduce the effects of adhesion.

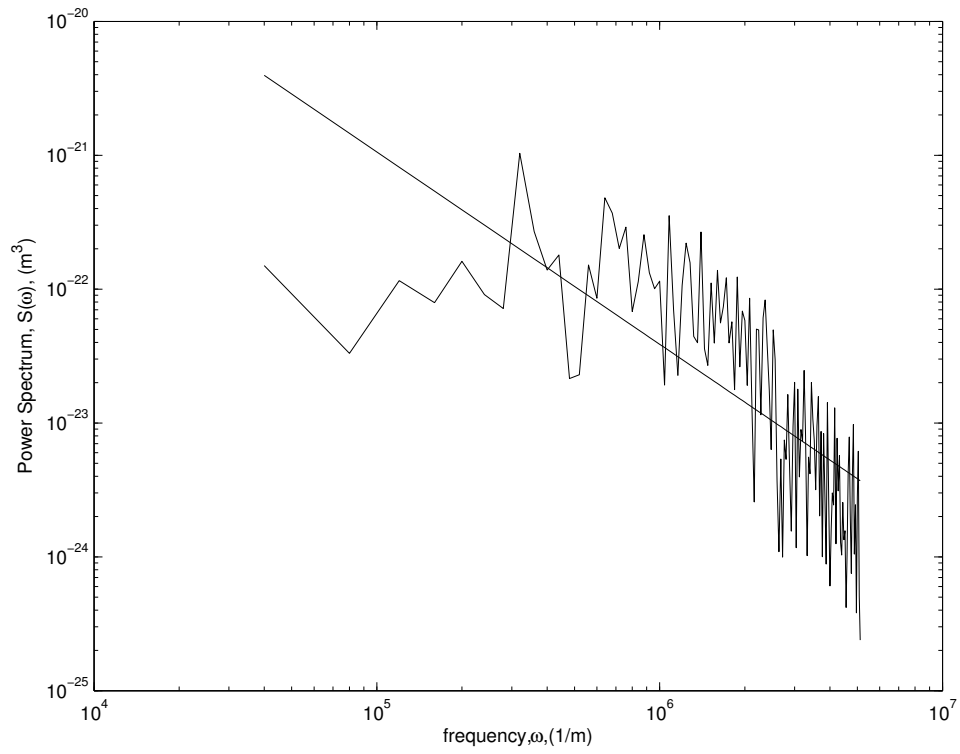


Figure 17: Power spectrum of equivalent rough surface.

The W-M function has several desirable characteristics which make it well suited to simulate rough surface topography. As mentioned previously, all surfaces exhibit roughness. When this roughness is continually magnified more roughness is revealed down to the atomic level. Therefore, mathematically stated, no unique tangent can be drawn at any point along the surface profile. This makes W-M an ideal candidate for surface topography simulation since it has the properties of being continuous everywhere and differentiable nowhere. Furthermore, each level of magnification appears similar in structure to the previous, thus the self-similarity leads to self-affinity.

In order to develop a contact theory based on fractal surfaces, a size or area distribution is needed for asperities in intimate contact. The concept of asperities in contact with an opposing surface is similar too the area of islands which are greater than a certain size. While studying the fractal nature of the coastline of England, Mandelbrot [30], proposed a power-law relationship which is given by:

$$N(S) = \left( \frac{S_l}{S} \right)^{D_s/2} \quad (4.3)$$

where  $N$  represents the number of islands that are greater than an area  $S$ . In Equation (4.3),  $D_s$  is the fractal dimension of the coastlines and  $S_l$  represents the area of the largest island. Majumdar [18] has argued that the coastal fractal dimension is similar to the fractal dimension  $D$  given in Equation (4.1). Therefore the size distribution can be determined by differentiation which gives:

$$\Gamma(S) = \frac{D}{2} \frac{S_l^{D/2}}{S^{D/2+1}} \quad (4.4)$$

This methodology is widely accepted in the literature in this field [18]-[24].

#### 4.4 ADHESIVE FRACTAL CONTACT MODEL

Utilizing fractal surface characterization and the adhesive contact solution given by JKR, an adhesive rough surface model will be developed that is valid over several length scales. Initially, the model will follow the example set forth by Majumdar and Bhushan [18]. In their work, it was assumed that the interference which a spherical asperity has with the rigid plane is given by:

$$\delta = G^{(D-1)}l^{(2-D)} \quad (4.5)$$

where  $l$  is identified by as the length scale of the asperity. In previous chapters the parameter  $\delta$  had referred to the *approach distance* between contacting spheres. Since the normal contact of spheres is physically analogous to the contact of a sphere with a rigid plane, the parameter  $\delta$  is now referred to as *interference* (the maximum displacement of an asperity). Figure (18) depicts the geometry of the truncated contact that of length scale,  $l$ . A relationship can be drawn between this length scale and the truncated area of the contact spot,  $l = (S')^{1/2}$ . It should be noted that any parameter shown with a superscript ‘prime’ refers to a truncated area. The subscripts ‘H’ and ‘JKR’ are used to denote Hertzian and JKR contact conditions respectively. Figure (19) schematically portrays the definition of the truncated area. From Hertzian contact theory, it is known that the truncated area is related to the real area of contact by the following relationship:

$$S_H = S'/2. \quad (4.6)$$

where  $S'$  is the truncated contact area. However, due to the inclusion of surface energy, none of the contacts in this chapter are of the Hertzian type. Using Equation (4.6), a relationship can be developed between the truncated area and the JKR contact area. Since this work will operate under a ‘fixed grips’ assumption, the interference distance must be equal for both the truncated and JKR conditions. Drawing upon Hertzian contact theory it is known that:

$$\delta_H = \frac{a_H^2}{R} \quad (4.7)$$

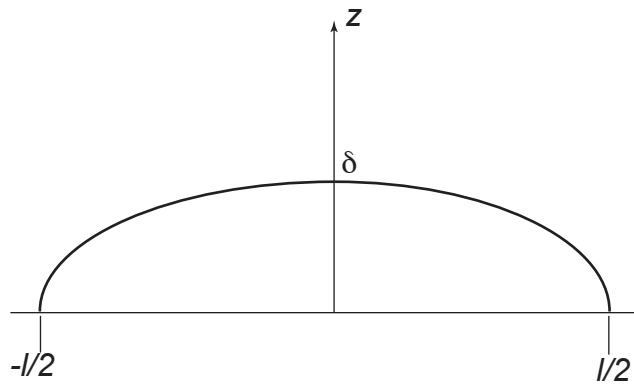


Figure 18: Geometry of contact spot with a given interference.

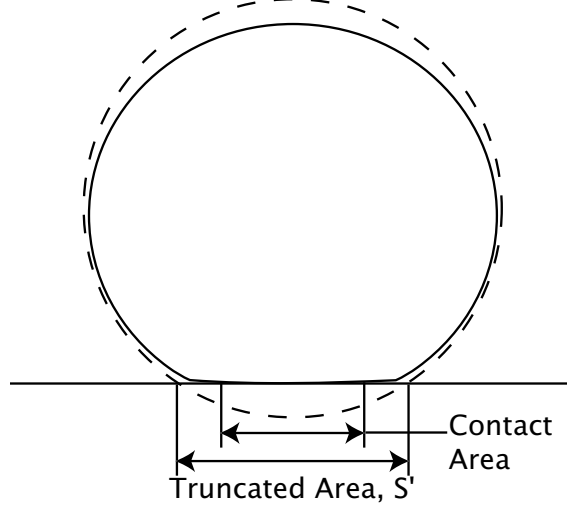


Figure 19: Truncated contact area depiction.

and from JKR theory:

$$\delta_{JKR} = \frac{a_{JKR}^2}{R} - \frac{2}{3} \sqrt{6 \left( \frac{w\pi a_{JKR}}{K} \right)}. \quad (4.8)$$

Equating equations (4.7) and (4.8) and using Equation (4.6), a relationship is developed which provides a means of conversion between the truncated and real contact area given by JKR theory:

$$S_{JKR} = 9.25 \left( \frac{S'^D G^{2(1-D)} w}{K} \right)^{2/3} \left( 1.68 - 0.61 \sqrt{5.95 - \frac{\sqrt{(S'\pi)/2}}{((S'^D G^{2(1-D)} w)/K)^{1/3}}} \right) \quad (4.9)$$

Majumdar and Bhushan neglected to note the difference between the real area of contact and the truncated area, but this was later exposed by Komvopolous in [23]-[25]. The following derivations will be in terms of the truncated area for simplicity of the expressions, but the results will be presented in terms of the real (JKR) area.

Following the work of Majumdar and Bhushan, the following assumption is made for the expression for the interference,  $\delta$ , in terms of the truncated area:

$$\delta = G^{(D-1)} (S')^{(2-D)/2} \quad (4.10)$$

Majumdar and Bhushan also provided an expression for the radius of curvature at the asperity tip, in terms of fractal parameters:

$$R = \frac{S'^{D/2}}{\pi^2 G^{D-1}}. \quad (4.11)$$

Using equations (4.10-4.11), relationships specific to asperities in the JKR contact regime can be developed. In this chapter, a rigid-flat plane that progressively approaches a randomly rough surface (see Figure (14)) will be analyzed. When a minimum distance is reached at point ‘a’, the rigid-flat plane will then be pulled away to point ‘b’. It is from this point ‘b’ that the system will be analyzed. During the separation phase under force control, a critical point is achieved at which the system becomes unstable and the surfaces will ‘jump’ apart. The force at this point is referred to as the critical pull-off force. In order to develop our analysis, the expressions for the critical stretch and contact area that are derived from JKR theory must be correlated to the fractal parameters  $G$  and  $D$ . An important contribution of the present analysis is the determination of  $S'_c$  as a function of only material and fractal parameters. The parameter  $S'_c$  represents the critical contact area just prior to the point of abrupt separation. This critical contact area allows for the study of the pull-off force as a function of separation distance.

Unlike Hertzian theory, asperities can sustain tensile tractions at the contact interface in JKR contact. Therefore, when the contacting surfaces are pulled away, the asperities are stretched. Equation (2.6) can be used to determine the magnitude of this stretching under fixed grip conditions. In Figure (20), the vertical tangent on the load deflection curve shows this point. Using Equation (2.6) and Equation (4.11), a relationship for the critical stress is given in terms of the fractal parameters and truncated area:

$$\delta_c = - \left( \frac{3w^2 S'^{D/2}}{4K^2 G^{D-1}} \right)^{1/3} \quad (4.12)$$

If the stretch becomes less than  $\delta_c$ , then adhesion is broken i.e.  $\delta_c < \delta$ . Therefore by substituting Equation (4.10) and Equation (4.12) into this inequality a relationship is found for the critical contact area:

$$S'_c = \left( \frac{3w^2}{4K^2} \right)^{\frac{1}{3-2D}} G^{\frac{4(1-D)}{3-2D}} \quad (4.13)$$

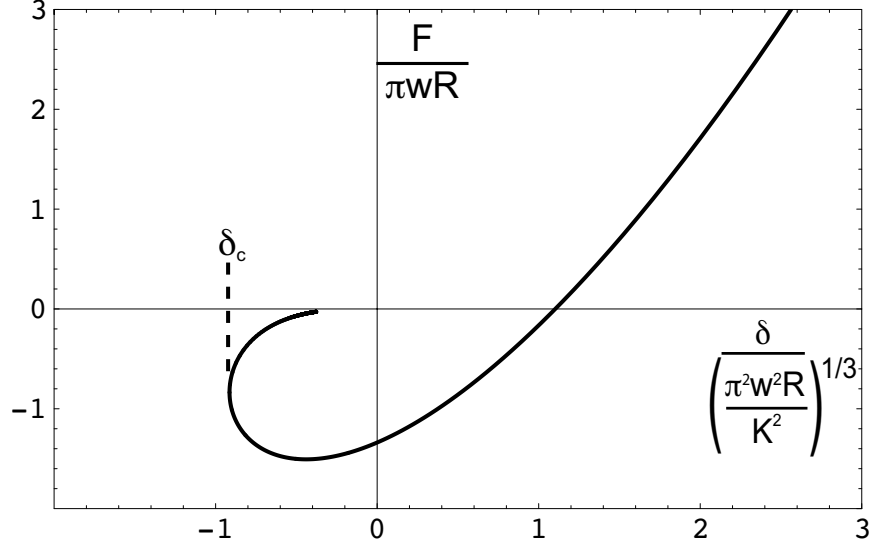


Figure 20: Load-Deflection curve for JKR theory

Equation (4.13) has a significant impact on asperity contact since it limits the size of the contact area for asperities when they are being stretched. For example, suppose that a relationship for the size distribution of the asperities,  $\Gamma(S')$ , is known. The following integral could then be used to give the real area of contact:

$$S'_{real} = \int_{S'_c}^{S'_l} S' \Gamma(S') dS' \quad (4.14)$$

Equation (4.14) is only valid for the contact condition of surfaces that are originally compressed together then subsequently separated. The parameter  $S'_l$  represents the area of the largest contact spot. It is important to note that the lower integration limit is not zero. This is due to the condition that no asperity can attain a contact area less than  $S'_c$ . Incidentally, Equation (4.14) is the exact relationship which is given in [18] for the contact area of asperities that are being deformed elastically. Therefore the integration in Equation (4.14) is carried out yielding the real-truncated area of contact,

$$S'_{real} = \frac{D}{2-D} \left( S'_l - S'_c{}^{1-D/2} S'_l{}^{D/2} \right) \quad (4.15)$$

To determine the pull-off force as a function of separation, the same premise used to produce Equation (4.15) can be used:

$$F = \int_{S'_c}^{S'_l} F(S')\Gamma(S')dS' \quad (4.16)$$

The load-contact radius relationship given by Equation (2.3) can be written entirely in terms of truncated area,  $S'$  using the conversion provided by Equation (4.9). Equation (4.16) can then be numerically integrated with the results of which will be presented in Section (4.5). It is noteworthy to mention that results of the numerical integration are not directly a function of separation distance but can be effectively controlled by  $S'_l$ . As the separation distance between the surfaces increases,  $S'_l$  decreases to a limit of  $S'_c$ .

## 4.5 RESULTS AND DISCUSSION

Utilizing the adhesion fractal contact model developed in Section (4.4), the adhesive forces between two surfaces can be analyzed as a function of surface roughness and interface material. The expressions (4.13), (4.15), and (4.16) allow direct manipulation and investigation of the influence of the fractal parameters  $G$  and  $D$ , and the material parameter,  $K$ . In the analysis presented in this section, a pair of micro-sized areas with an apparent area of  $S_{app} = 625\mu m^2$ , and a combined work of adhesion of  $w = .1J/m^2$  will be assumed (see Table 6). In order to demonstrate the applicability of the expressions derived in Section (4.4), results will be generated by varying the fractal parameters ( $D$  and  $G$ ) and the effective modulus,  $K$ . Table 6 indicates the various conditions explored. These conditions were chosen because they produce a circumstance where JKR theory is applicable. Let us first investigate the effects that varying the fractal parameter  $D$  has on the adhesive forces. As mentioned previously, the system being analyzed is under displacement control so that the separation distance between the two surfaces can be controlled by increasing or decreasing  $S'_l$ . Since we are concerned with the adherence force,  $S'_l$  can be decreased until the limit of  $S'_c$  is attained, thereby revealing the critical pull-off force. This is determined by allowing  $S'_l$  to range from the critical adhesion contact area,  $S'_c$ , to values much larger than  $S'_c$ , for different  $D$  values. Curves can then be generated for each  $D$  value by parametrically varying  $a'_l$  and plotting

Table 6: Conditions for numerical results.

Case	$D$	$G \times 10^{-14}$ (m)	$K \times 10^8$ Pa
1	1.320, 1.319, 1.318	1.0	117
2	1.320	1.0, 1.2, 1.5	117
3	1.320	1.0	112,115,117

equations (4.15) and (4.16) in nondimensional form as shown in Figure (21). As depicted in the figure, the critical pull-off force can be determined by the vertical tangent of each area load curve, as labeled by the symbol  $F_c$  for  $D=1.32$ . An important tendency exhibited by Figure (21) is that overall pull-off force increases with the fractal dimensional parameter  $D$ . The underlying explanation for this phenomenon is found by examining the surface topography at different fractal dimensional values, as illustrated in Figure (22) and Figure (23).

It is important to note that  $D = 1.2$  and  $D = 1.4$  were chosen in Figure (22) and Figure (23) to highlight the effects of varying  $D$ , and do not directly correspond to the values shown in Figure (21). As illustrated in these figures, increasing the value of  $D$  at a fixed  $G$  value dramatically changes the surface profile. Specifically, as  $D$  increases, the density of the asperities becomes greater, while the overall surface roughness becomes smoother because of smaller asperity heights. For a higher asperity density, the number of adhesive contact interactions between surfaces will be greater, therefore increasing the energy required for separation. Since the disparity in asperity heights also decreases with the increase of  $D$ , the elastic energy stored in the compressed asperities will be less dominant than the adhesive energy in the stretched asperities (when compared to lower  $D$  values). Since these factors will decrease the amount of elbowing along the contact interface, the increase in pull-off force with increasing  $D$  shown in Figure (21) can be accounted for.

Turning our attention to the fractal parameter,  $G$ , Figure (24) illustrates the influence that varying  $G$  has on the adhesive forces. Examining the figure, it is clearly shown that the critical pull-off force substantially increases with decreasing  $G$  values. To understand this tendency, Figure (25) was generated to illustrate how the surface topography varies with

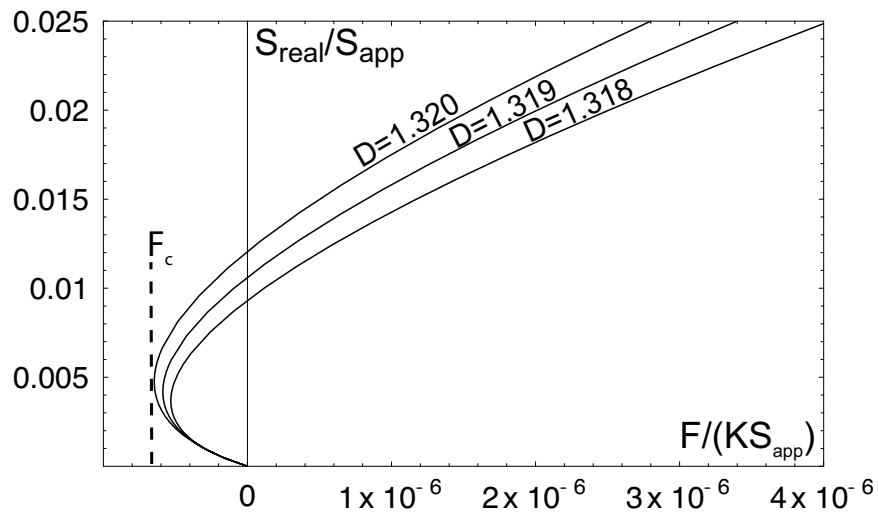


Figure 21: Effect of fractal parameter  $D$  on pull-off force

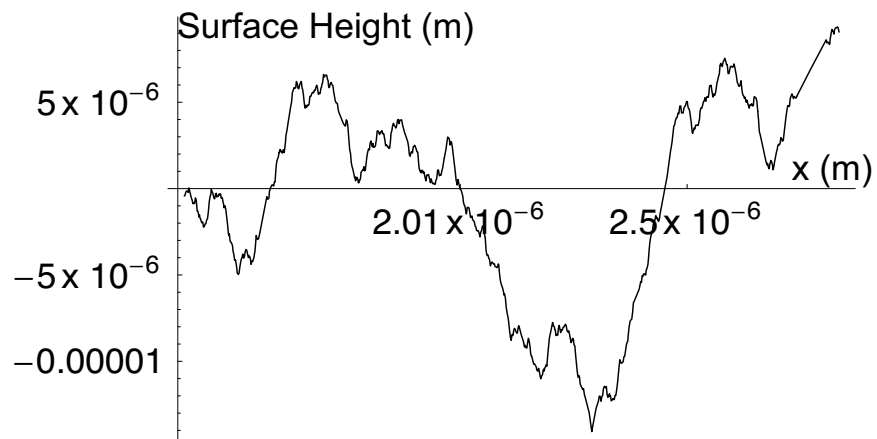


Figure 22: Fractal parameter  $D=1.2$ .

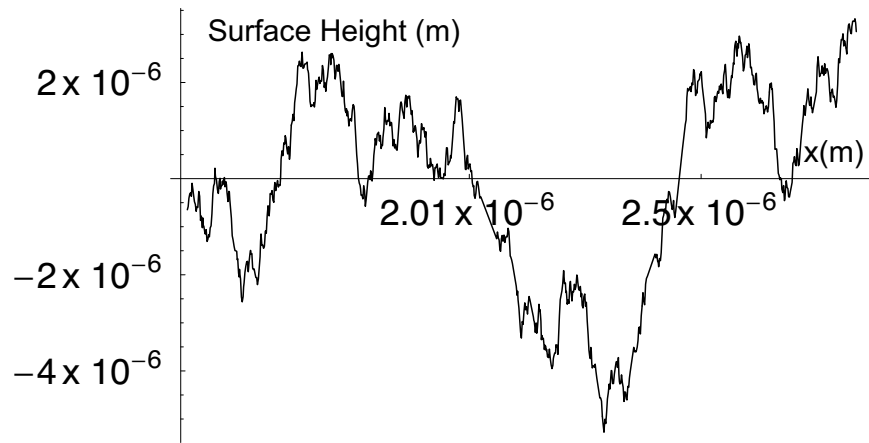


Figure 23: Fractal parameter  $D=1.4$ .

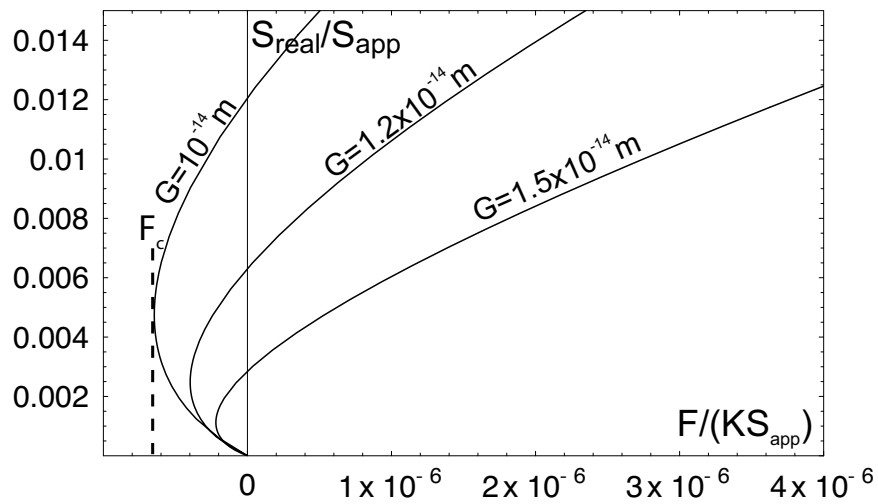


Figure 24: Effect of fractal parameter  $G$  on pull-off force

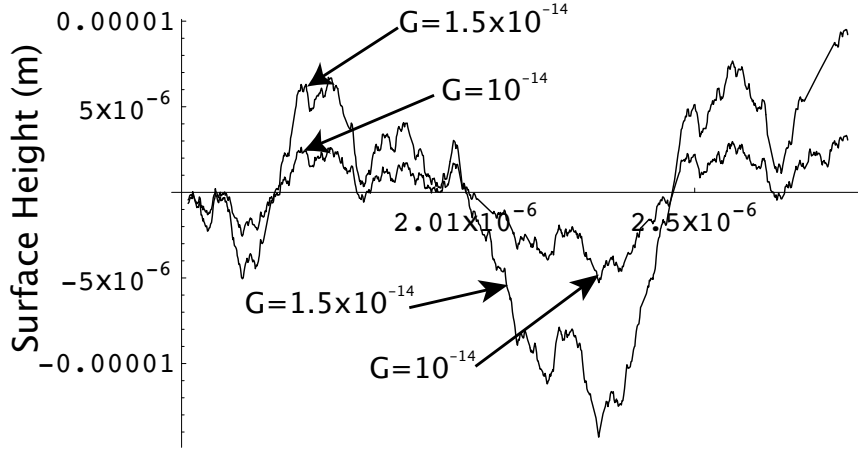


Figure 25: Effect of  $G$  on surface topography.

$G$ . As indicated in Figure (25), increasing the values of  $G$  amplifies the magnitude of the asperity peaks. Again considering the influence of elbowing, the greater the magnitude of the asperity peak heights, the more elastic energy that will be stored between the contacting surfaces for a give separation distance. Hence, at larger  $G$  values, there will be more elastic restoring energy to force the contacting surfaces apart, which will decrease the critical pull-off force, as shown in Figure (24).

Finally, the influence that the material parameter  $K$  has on the pull-off force is demonstrated in Figure (26). As shown in the figure, the total load and critical pull-off force decreases with increasing  $K$ . Since  $K$  is a measure of the equivalent elastic modulus of the contacting surfaces, a large value of  $K$  indicates that the contact interface is stiff. Therefore, the amount of restoring force between asperities will directly increase with  $K$ , as indicated by the lower critical pull-off force magnitudes at higher  $K$  values in Figure (26).

Two factors govern the validity of these results: *i*) asperities are not interacting with one another, that is, the real to apparent contact area is small, *ii*) the asperities in contact are in the JKR regime. Both of these conditions are satisfied in the present analysis. To address item *i*, the ratio of the real and apparent area of contact for the variables examined is less than five percent, which indicates that the asperity interaction is small. Considering item *ii*, the we can examine the Tabor parameter  $\mu$  for these conditions. The Tabor parameter  $\mu$

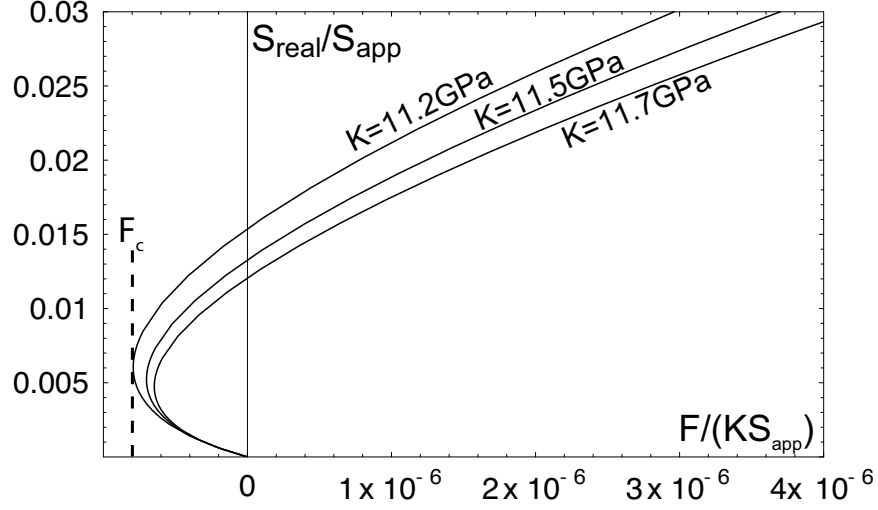


Figure 26: Effect of varying effective elastic modulus,  $K$ , on pull-off force

is defined by:

$$\mu = \left( \frac{Rw^2}{K^2 z_o^3} \right)^{1/3} \quad (4.17)$$

Written in terms of the fractal parameters, this relationship becomes:

$$\mu = \left( \frac{wS^{D/2}}{\pi^2 K^2 z_o^3 G^{D-1}} \right) \quad (4.18)$$

From Equation (4.18), the  $\mu$  values in our analysis range from approximately 3 to 4.5. Based on the work of Johnson and Greenwood [31], it has been shown that JKR theory applies to  $\mu$  values as low as 1.0. Therefore the presented trends are well within the acceptable limits to produce valid results.

## 4.6 SUMMARY AND CONCLUSIONS

In the present chapter a closed form analytical solution has been determined for adhesive rough surface contact in terms of fractal parameters. This solution can be applied to any surface interface provided that estimations can be obtained for the work of adhesion, and the fractal parameters  $G$  and  $D$ . With the growing popularity of MEMS technology, there is an inherent need to more accurately characterize the pull-off force using a methodology that is independent of length scale. The developed expressions provide a mechanism to perform this characterization by directly coupling the elastic deformation and adhesive effects within the contact interface. In addition to improving accuracy, the presented expressions are potentially useful for MEMS designers because they allow determination of adhesive forces as a function of easily obtainable parameters.

To illustrate the usefulness of the developed expressions, the influence of the fractal parameters  $G$  and  $D$ , and the material parameter  $K$  on the adhesive forces were analyzed. Based on this analysis, the following trends were determined:

1. The critical pull-off force increases with the fractal parameter  $D$  due to the greater density of asperity peaks at larger  $D$  values.
2. The critical force required for separation decreases with increasing  $G$  because of the larger asperity peaks and the increased elbowing that occurs at higher  $G$  values.
3. Increasing the effective modulus along the contact interface reduces the effects of adhesion due to the greater level of elastic energy stored in the asperities.
4. Small variations of the fractal parameter  $G$  has the most significant impact on the variation of pull-off force.

## 5.0 FRACTAL CONTACT MODEL FOR JKR-DMT SOLUTION REGIME

### 5.1 INTRODUCTION

In chapter 3 and chapter 4 there have been several limiting assumptions which dictated the generality of the solution. First in chapter 3, the radius of curvature for the contacting asperity is assumed prior to contact force and area determination. Therefore inherent to the statistical based solution method a length scale is assumed. To accommodate surfaces which exhibit roughness on several length scales, an adhesive fractal solution based on JKR contact types was presented in chapter 4. Although the applicability of this solution is extended to multi-scale surfaces, the contact type was limited to JKR contact. In this present chapter the most general of all adhesive rough surface solution methods is presented. The surface characterization is based on a three-dimensional characterization and the contact type is determined at the time of integration. Although the method is shown for isotropic surface roughness, it can easily be extended to anisotropic surface roughness.

### 5.2 3-D ROUGH SURFACE SIMULATION

Rough surface contact solutions are traditionally implemented in a two stage process. First, the topography is characterized by either a statistical or a fractal method. Secondly, an assumption is made that the peaks in contact can then be modeled by simplified shapes such as spheres. By performing these steps, it can be established which asperities are in intimate contact and which are not. By determining the interference or deformation that each asperity incurs, the total contact area and load can be subsequently calculated. A

similar methodology will be used in the present analysis in our adhesive surface contact algorithm.

In this chapter, a fractal surface geometry (see chapter 4) will be used to characterize the topography. A fractal geometry was chosen because most engineering surfaces have been shown to exhibit roughness on several different length scales. If for example, one would attempt to characterize a multi-scale surface with traditional statistical parameters such as average surface roughness, slope and curvature, they would render different results depending on the scale at which the measurements were taken. Fractal geometry, on the other hand, offers a uniquely defined set of parameters which are invariant with respect to scale. More specifically, once the scale-invariant fractal parameters are determined, the roughness can be predicted at all length scales for which the surface is shown to exhibit fractal behavior [17].

In the present investigation, it will be assumed that the surface roughness is isotropic. Physically, this means that if scans were made in the two lateral directions  $x$  and  $y$ , the characteristic fractal parameters would be the same. In order to obtain actual fractal parameters, a scan is taken which reveals the profile of the surface at a particular cross-section. Once the profile is obtained, for a surface, its power spectrum density (PSD) is determined using a fast fourier transform (FFT). When the PSD of the profile is plotted versus frequency on log-log scale, a linear relationship is revealed for surfaces which exhibit fractal behavior. For the Weierstrass-Mandelbrot (W-M) function,

$$z(x) = G^{D-1} \sum_{n=n_l}^{\infty} \frac{\cos(2\pi\eta^n x)}{\eta^{(2-D)n}} \quad (5.1)$$

Berry and Lewis [29] show that the power spectrum is given by:

$$P(\omega) = \frac{G^{2(D-1)}}{2 \ln(\eta)} \frac{1}{\omega^{(5-2D)}}. \quad (5.2)$$

In Equations (5.1 & 5.2)  $D$  and  $G$  are the fractal roughness and scaling parameters. These two scale invariant parameters are found by respectively determining the slope and intercept point from the log-log plot of the PSD. The fractal roughness parameter  $D$  varies from one to two and is dimensionless, while the scaling parameter  $G$  is not limited to a specific range and carries a length dimension. In Equation (5.2), the density of asperities,  $\eta$ , must be greater than one. A review of the literature ([18], [3], [24]), however, reveals that  $\eta$  is typically taken

as 1.5. The physical significance of the fractal parameters  $G$  and  $D$  are explained as follows. As  $D$  becomes larger, the number of asperities increase and their heights decrease. By this definition, as  $D$  approaches 3.0, the surface will become smoother. Therefore, as explained in [32],  $D$  governs the contribution of the low and high frequency components to the surface. The parameter  $G$  is referred to as the fractal roughness. As  $G$  increases, the peaks and valleys are amplified, such that the asperity peaks are higher and the valleys are lower.

In this chapter, the contact interface of two actual MEMS components will be analyzed to demonstrate the use of the adhesive surface contact algorithm. The surface profiles were obtained by taking scans of LIGA surfaces using an atomic force microscope (AFM). As shown in Figure (27), the AFM profile taken from the first surface exhibits a randomly rough topography with periodic ribs which were manufactured to reduce the effects of adhesion. In Figure (27), the solid profile corresponds to the actual AFM scan and the dashed line represents the fractal simulation of the profile. Apart from the ribs, the roughness predicted by the fractal profile accurately models the topographical features of the scanned geometry. Likewise, Figure (28) depicts the AFM profile and fractal representation of the second fractal surface. As with Figure (27), Figure (28) shows that the second surface is randomly rough and is adequately modeled by the fractal representation.

To simulate the contact between the surfaces in figures 27 and 28, the concept of an equivalent rough surface will be utilized. To obtain an equivalent surface, the PSD is first determined for both surfaces (solid profiles in figures 27 and 28). The power spectra are then summed together and plotted versus frequency so that the fractal parameters  $G$  and  $D$  can be obtained for the equivalent rough surface. With the equivalent fractal representation, the rough surface interface can be replaced by an equivalent rough surface and a smooth rigid plane, as discussed in Section (3.4). Figure (17) in chapter 4 depicts the equivalent power law relationship between the PSD and frequency for the two LIGA surfaces being analyzed in this chapter. It should be noted that when converting the fractal parameters from profile to surface parameters, the fractal scaling parameter,  $G$ , remains the intercept point of Figure (17). The fractal roughness parameter,  $D$ , however must be increased by one [18]. Hence, for an equivalent surface, the range for  $D$  will be between two and three. For the composite PSD shown in Figure (17) for the actual LIGA surface investigated in

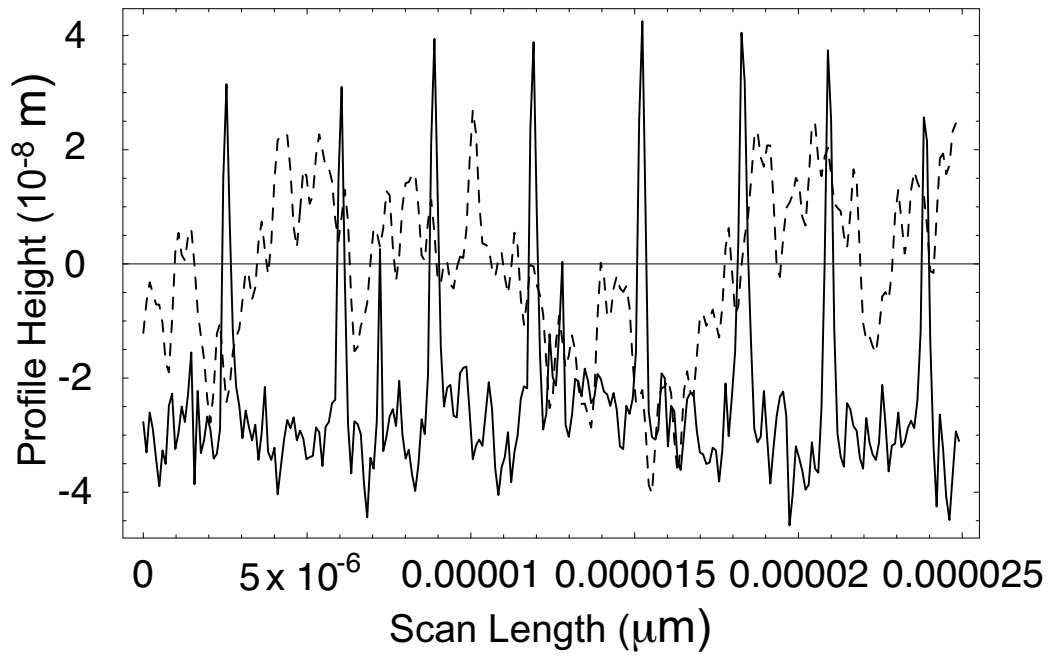


Figure 27: Typical AFM scan of ribbed LIGA surface.

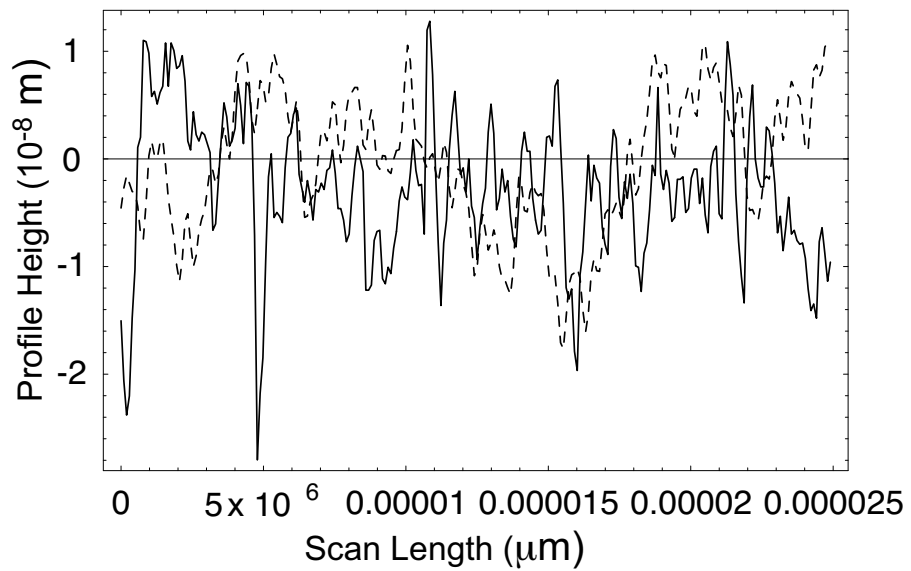


Figure 28: AFM scan of mating LIGA surface.

this chapter, the slope and intercept were respectively found to be 1.7815 and  $1.3152 \times 10^{-9}$  meters, which yields equivalent surface  $D$  and  $G$  values of 2.7815 and  $1.3152 \times 10^{-9}$  meters.

In order to generate surface topography information directly from the above fractal parameters, a multivariate fractal version of the W-M function given by Ausloos and Berman was utilized [33]. In their work, Ausloos and Berman demonstrated that the W-M function could be a function of more than one variable. Yan and Komvopoulos [34] then presented a version of Ausloos and Berman's function that was readily applicable for use with rough surface contact theory [34, 3, 32]. The three-dimensional version of the Ausloos and Berman function is given by [34]:

$$z(x, y) = L \left( \frac{G}{L} \right)^{D-2} \left( \frac{\ln \eta}{M} \right)^{1/2} \sum_{m=1}^M \sum_{n=0}^{n_{max}} \eta^{D-3n} \left( \cos \phi_{m,n} - \cos \left[ \frac{2\pi \eta^n (x^2 + y^2)^{1/2}}{L} \cos \left( \tan^{-1} \left( \frac{x}{y} \right) - \frac{\pi m}{m} \right) + \phi_{m,n} \right] \right) \quad (5.3)$$

where  $z(x, y)$  represents the asperity height at each  $x - y$  location,  $\eta$  determines the density of frequencies,  $L$  is the sample length,  $M$  is the number of superimposed ridges,  $D$  is the fractal dimension ( $2 < D < 3$ ),  $G$  is the fractal roughness, and  $\phi_{m,n}$  are random phases. The parameter  $n_{max}$  is related to the maximum frequency by the following relationship,

$$\eta^{n_{max}} = L/L_s \quad (5.4)$$

where  $L_s$  is 'cut-off length' (which is the instrument resolution). The parameter  $n_{max}$  is determined by solving Equation (5.4) and taking the integer value of the ratio  $\log(L/L_s)/\log(\eta)$ . Utilizing Equation (5.3), a contour plot can be generated directly from the fractal parameters. Figure (29) shows a contour plot of the equivalent surface being analyzed in this work ( $D = 2.7815$  and  $G = 1.3152 \times 10^{-9}$  meters).

In order to verify that the topography shown in Figure (29) is representative of an isotropic fractal surface, a two-dimensional power spectrum can be taken (see Figure (30)). For isotropic behavior, the resultant plot of should reveal an axi-symmetric power spectrum. In the case of Figure (30), it is seen that the two-dimensional power spectrum exhibits axial symmetry [34]. It is important to mention that as found by Anguiano *et al* [35], the two orthogonal bands seen along the frequency axes are artificial and can be eliminated.

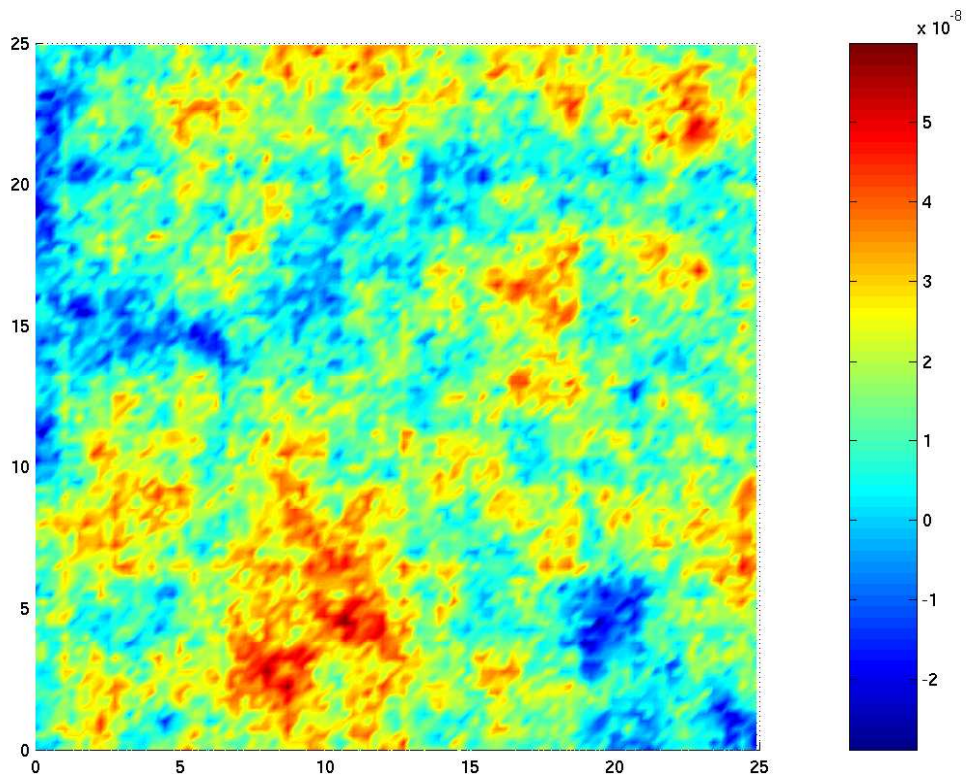


Figure 29: Contour plot of surface topography for simulated surface.

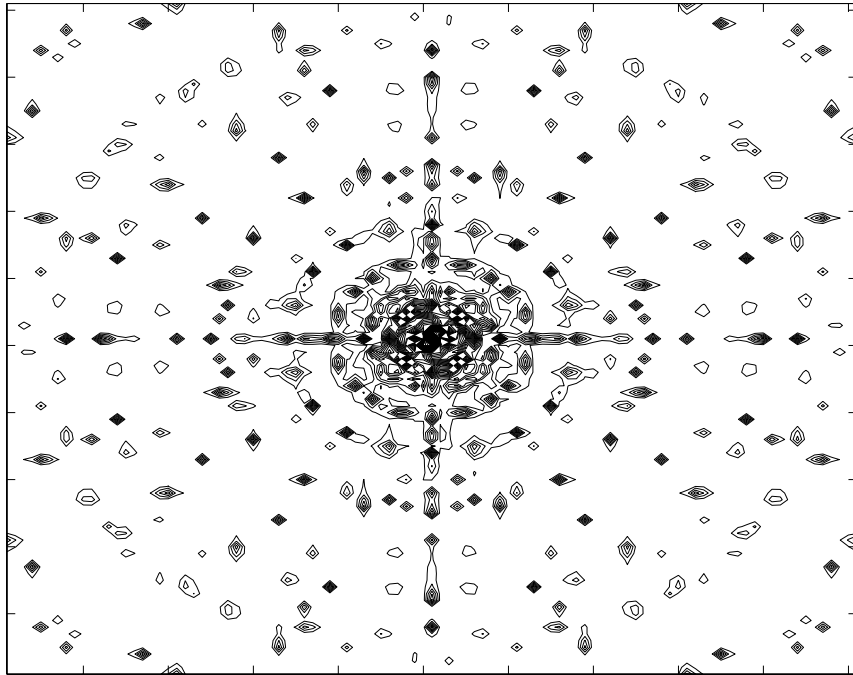


Figure 30: Axi-symmetric power distribution of simulated surface.

## 5.3 ADHESIVE ROUGH SURFACE SOLUTION METHODOLOGY

### 5.3.1 BACKGROUND

Before describing the algorithm developed in this chapter in detail, it is important to review the work of Yan and Komvopoulos [34] to provide an adequate background of the equations utilized. In their work a three-dimensional rough surface analysis was conducted for elastic-plastic materials. The expressions developed by Yan and Komvopoulos were useful in the present algorithm. In order to develop easy to use expressions for the asperity interference, Yan and Komvopoulos developed a two-dimensional form of Equation (5.3) to account for the  $M$  number of ridges by introducing a multiplicative factor which was eventually set equal to 1. This implied that a two-dimensional W-M function could be used to approximate a fractal function in three dimensions. By making these approximations, the following expression is developed:

$$\delta = 2G^{D-2} \ln \gamma^{1/2} (2a')^{3-D}. \quad (5.5)$$

Yan states in [34] that since the radius of curvature of each asperity is much greater than the height of the asperity then this relationship can be assumed to be

$$a'^2 = 2R\delta \quad (5.6)$$

where  $a'$  is the truncated contact radius. He then uses Equations (5.5 & 5.6) to find a relationship for the radius of curvature as a function of the truncated area and fractal parameters:

$$R = \frac{S'^{(D-1)/2}}{2^{(5-D)} \pi^{(D-1)/2} G^{(D-2)} (\ln \eta)^{1/2}} \quad (5.7)$$

where  $S'$  is the truncated contact area. Throughout the remainder of this chapter, primed variables correspond to ‘truncated’ values. The fractal relationship for the radius of curvature,  $R$  can be used to modify the Equation (1.5) to give a transition parameter which is related to fractal dimensions

$$\lambda = 1.16 \left( \frac{w S'^{(D-1)/2}}{2^{5-D} K^2 \pi^{(D-1)/2} G^{D-2} \sqrt{\ln \eta} z_o^3} \right)^{1/3} \quad (5.8)$$

Since in Equation (1.5)  $\sigma_o$  is not an easily attainable value, the relationship between  $\lambda$  and Tabor's transition parameter is used:

$$\lambda = 1.16\mu \quad (5.9)$$

where  $\mu$  is defined by:

$$\mu = \left( \frac{Rw}{K^2 z_o^3} \right)^{1/3} \quad (5.10)$$

where  $z_o$  is the intermolecular distance, which is about 0.3 – 0.5 nm. With this background, the truncated area can now be determined based on a given interference. By substituting Equation (5.7) into Equation (5.6), the following expression is used to solve for the truncated area based on interference for each  $i$ th asperity:

$$\frac{S'_i}{\pi} = 2 \left( \frac{S'_i{}^{(D-1)/2}}{2^{(5-D)} \pi^{(D-1)/2} G^{(D-2)} (\ln \gamma)^{1/2}} \right) \delta_i \quad (5.11)$$

Equation (5.11) can be solved using a fixed point iteration scheme to determine the truncated area. It should be noted that the truncated area is used for the first iteration of the algorithm (see next section) only. For efficiency and to reduce solution time, the previously converged area for each asperity is saved and is subsequently used as the starting point for the next level of interface separation.

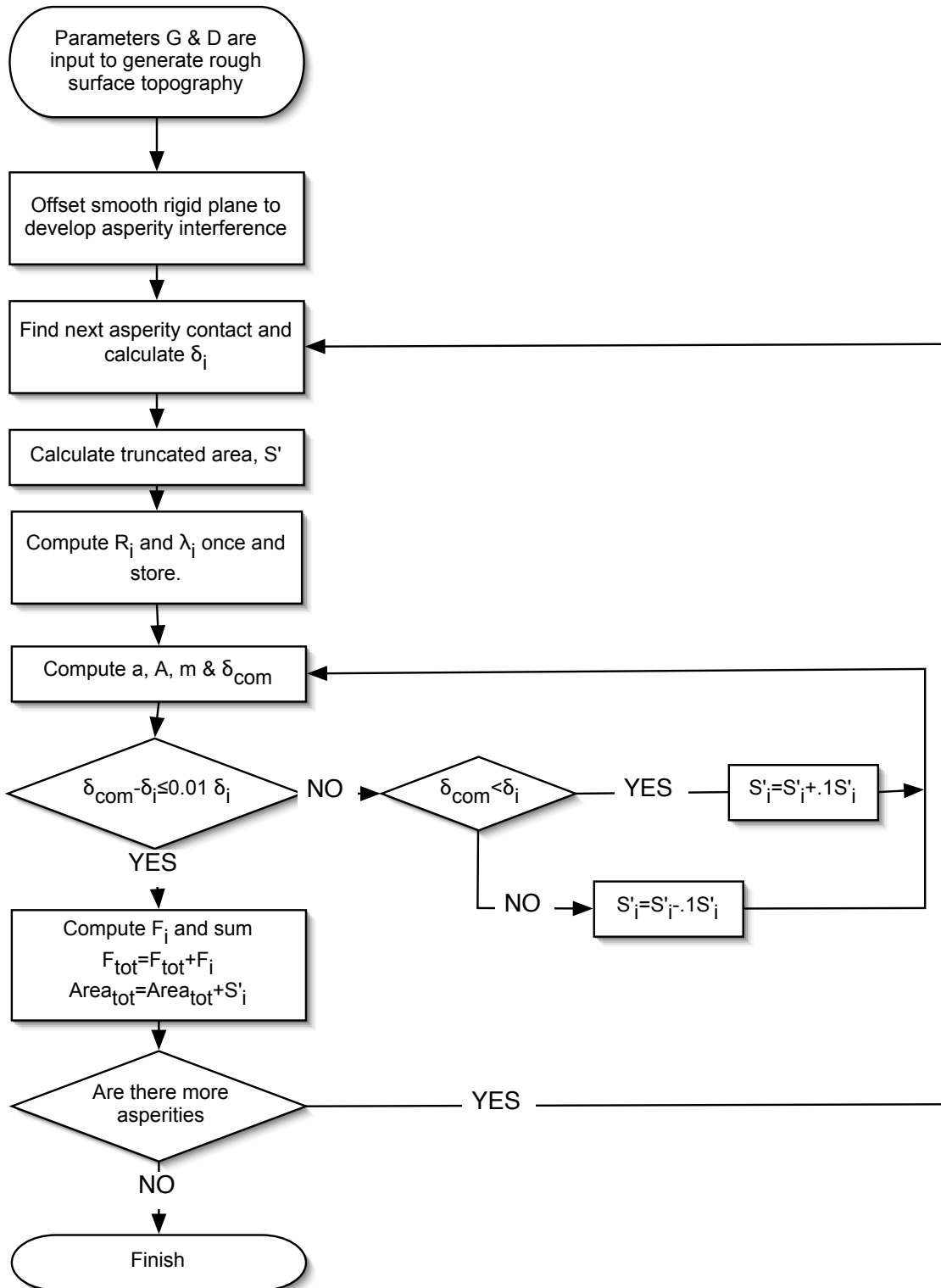


Figure 31: Iterative scheme to solve for total load and area.

### 5.3.2 ALGORITHM

To solve for the total load and contact area a novel numerical algorithm has been developed. In this algorithm the Maugis-Dugdale solution, introduced in Section (2.2), is used to model the micro-sized contact of each asperity. Unique to the methodology presented in this chapter is that there is no assumption of length scale or contact type prior to load and contact area integration. The transition parameter is uniquely determined for each asperity based on the given contact conditions. Furthermore, with the use of a fractal characterization, the surface topography can be modeled in a scale-invariant manner.

This algorithm is described in a flowchart format shown in Figure (31). As described in the figure the first step is to generate the surface topography from the fractal parameters using Equation (5.3). Next the surface is offset to introduce an initial penetration into the rigid plane. The interference,  $\delta_i$ , of each asperity is determined. Based on this interference, the truncated area is subsequently computed for only the asperities that are physically interfering with the rigid plane. As described in chapter 4, the ‘truncated area’ is the area of intersection between the flat plane and the spherical capped asperity (see Figure (19)). The truncated area is then used to compute the radius of curvature and transition parameter  $\lambda$  for each asperity. Once the values for  $\lambda$  and  $R$  values are found from the initial interference, they are stored for later use during subsequent calculation of the mean interface separation.

Once the truncated area is initially determined, the main iteration scheme is started to determine the real area of contact for each asperity. Using the values for  $R$  and  $\lambda$ , the contact radius,  $m$  and  $\delta_{com}$  are computed. These values are computed based on the adhesive contact solution of Maugis [5], (see Section (2.2)) given in equations (2.7-2.9).

$$1 = \frac{\lambda A^2}{2} [\sqrt{m^2 - 1} + (m^2 - 2) \arctan \sqrt{m^2 - 1}] \\ + \frac{4\lambda^2 A}{3} [(\sqrt{m^2 - 1} \arctan \sqrt{m^2 - 1}) - m + 1]$$

$$\Delta = A^2 - \frac{4}{3} A \lambda \sqrt{m^2 - 1}$$

$$\bar{F} = A^3 - \lambda A^2 \left( \sqrt{m^2 - 1} + m^2 \tan^{-1} \sqrt{m^2 - 1} \right)$$

where  $A$ ,  $\Delta$ , and  $\bar{F}$  are defined by:

$$A = \frac{a}{(\pi w R^2 / K)^{1/3}}$$

$$\Delta = \frac{\delta}{(\pi^2 w^2 R / K^2)^{1/3}}$$

and  $\bar{F} = F/(\pi w R)$ . The algorithm first calculates the contact radius,  $a'$ , using the relationship  $\sqrt{S'/\pi}$ .  $S'$  could either be the truncated area (during the first step) or the converged contact area from a previous sub-step. From the contact radius,  $A$ , is calculated and used in Equation (2.7) to solve for  $m$ . Based on the values for  $A$  and  $m$ , the computed approach  $\delta_{com}$  is solved for using Equation (2.9). If the percent difference of  $\delta_{com}$  is less than one percent then the iteration has converged. If  $\delta_{com}$  is not sufficiently close to the prescribed approach, however, the value of  $S'$  is adjusted. In the event that  $\delta_{com} < \delta$ , then  $S'$  is increased, whereas if  $\delta_{com} > \delta$  the area is decreased. The iterations will continue in this manner until convergence has been reached. Once the iterations have converged, the values of the load,  $F_i$ , and area,  $S_i$  are added to the totals ( $F_{total}$  and  $S_{total}$ ). All interfering asperities are iterated on in this fashion and then the surface is moved to the next separation location and the procedure starts once again.

## 5.4 RESULTS

The solution methodology outlined in Section (5.3) was implemented in *Mathematica*. The validity of the this solution scheme was first established by examining the contact of a single asperity. For this condition, the results predicted by our algorithm can be measured against Maugis' single asperity solution. Figure (32) shows a comparison between both the numerical result and the MD solution for  $\lambda = 4.815$  and  $\lambda = 0.498$ . In the figure, that the diamond and starred shaped icons represent our numerical results while the solid lines are Maugis' solution. Examining the curves depicted in Figure (32), it is found that our numerical scheme predicts results nearly identical to Maugis' theory at both high and low values of  $\lambda$ . Such a trend indicates that our algorithm is able to accurately predict the contact behavior for a wide range of values of the transition parameter,  $\lambda$ .

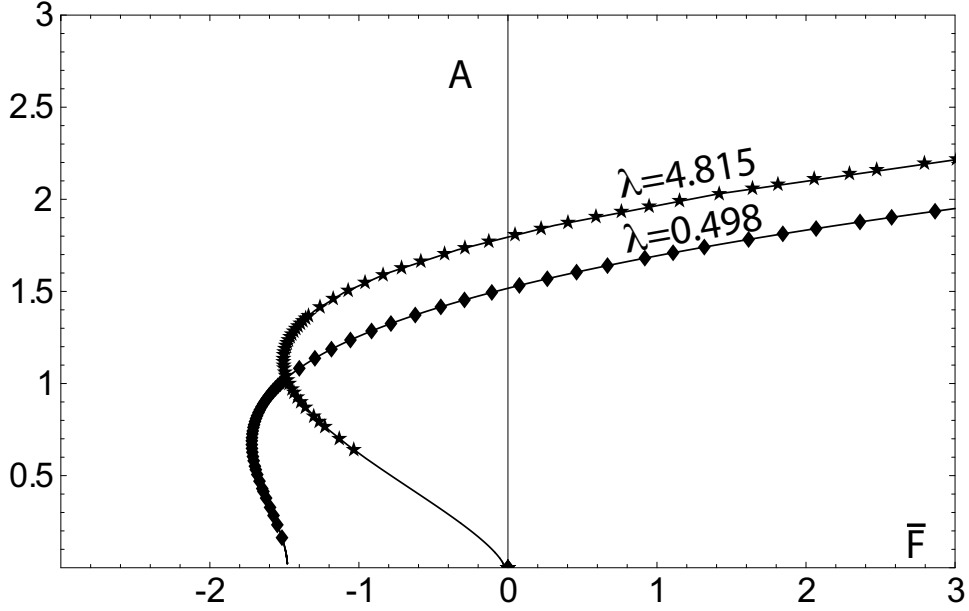


Figure 32: Single asperity validation of algorithm.

After being validated, the method described in Section (5.3) was used to examine several factors that influence the pull-off force. In this section we will specifically examine the influence of the material stiffness, the work of adhesion, and the topography parameters  $G$  and  $D$ . The material and surface topography parameters for all of the numerical investigations conducted are listed in Table 7. The LIGA nickel material whose surface geometry was described in figures 27 and 30 was used in all analyses. LIGA nickel was specifically chosen due to its manufacturability and growing popularity for the construction of micro-scale devices. In the analyses, it was assumed that both contacting rough surfaces were constructed of nickel. Using Equation (1.4) the compliance can thereby range from 70.3 GPa to 110.3 GPa [36]. The surface energy of nickel was found to be  $2280 \text{ mJ/m}^2$  [37], which makes the work of adhesion approximately  $4 \text{ J/m}^2$ . This value of  $w$  should be considered an upper limit in the present analysis. Because there is much discrepancy between the theoretical work of adhesion values and those determined from experiments, the present investigation will assume a moderate value of  $0.25 \text{ J/m}^2$  for the bulk of the numerical simulations. The fractal scaling parameter  $G$  was chosen to range between  $0.9152 \times 10^{-9}$  and  $5.3152 \times 10^{-9}$  meters, and the fractal roughness parameter  $D$  was selected to vary from 2.6815 to 2.8815.

Table 7: Operating conditions for the investigation of individual parameters.

Case	$K$ (GPa)	$w$ (J/m <sup>2</sup> )	$D$	$G$ ( $\times 10^{-9}$ )m
1	110.3, 90.3, 70.3	0.25	2.7815	1.3152
2	110.3	0.05, 0.15, 0.25	2.7815	1.3152
3	110.3	0.25	2.6815, 2.7815, 2.8815	1.3152
4	110.3	0.25	2.7815	0.9152, 1.3152, 5.3152

The following parameters were held constant for all numerical simulations:  $S_a = 620.1 \mu\text{m}^2$ ,  $L = 24.9 \mu\text{m}$ ,  $L_s = 1.47 \times 10^{-9}$ ,  $\eta = 1.5$  and  $M = 10$ . It should be noted that using the numerical method presented in this chapter along with experiments, however could enable a researcher to determine the real area of contact based on the determined work of adhesion by changing values of  $w$  to account for varying degrees of adhesion.

Considering first the influence that the interface stiffness,  $K$ , has on adhesion forces, the ratio of real to apparent contact area was plotted versus total load in Figure (33). The normal force results are plotted as a function of  $\delta_{mean}/\sigma$ , where  $\delta_{mean}$  is defined as the distance between rigid plane and average asperity peak height. The parameter  $\delta_{mean}$  then non-dimensionalized by the average roughness of the asperity peaks. As depicted, the interface stiffness considerably increases as the adherence force decreases. Physically, the increased stiffness causes the larger asperities (ones with more interference) to produce a compressive force which dominates the adhesion in the shorter stretched asperities. In fact Figure (33) illustrates the ‘elbowing effect’ discussed by Johnson [1]. In the figure, it is shown that elbowing can become markedly more dominant as the interface stiffness increases.

Investigating the role that varying the work of adhesion has on our system, Figure (34) depicts that as the surface energy is increased, the adherence force becomes stronger. This is to be expected because at a higher surface energy, each asperity has more adhesive energy, thereby causing an increased force to separate the two surfaces. Further examination of Figure (34) an obvious yet important result for designers: to minimize stiction forces in mating micro-components, the energy of the interface should be reduced. This can be accomplished by choosing materials which have a high interface energy,  $\gamma_{12}$ , thereby reducing the overall

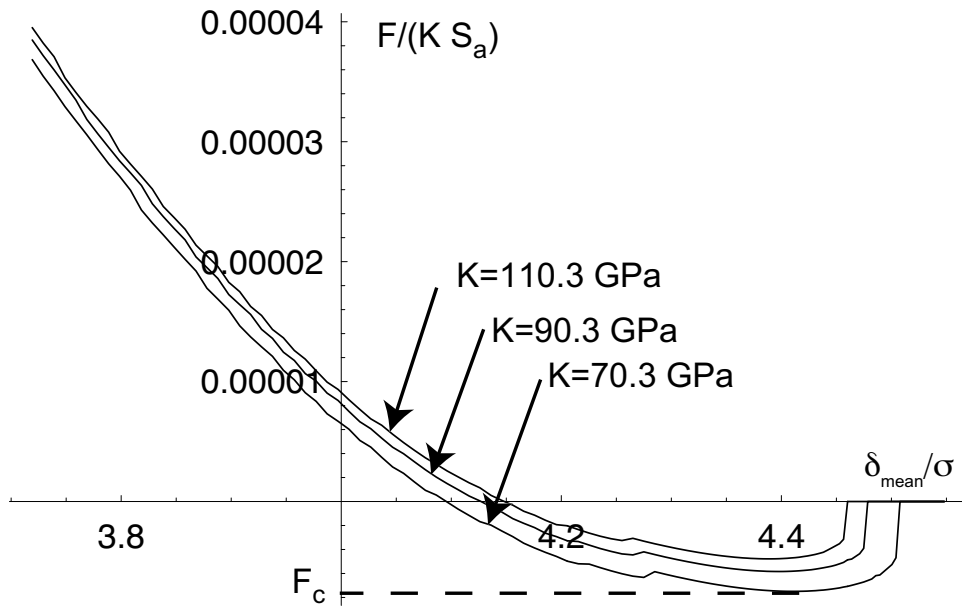


Figure 33: Effect of varying stiffness on adherence force.

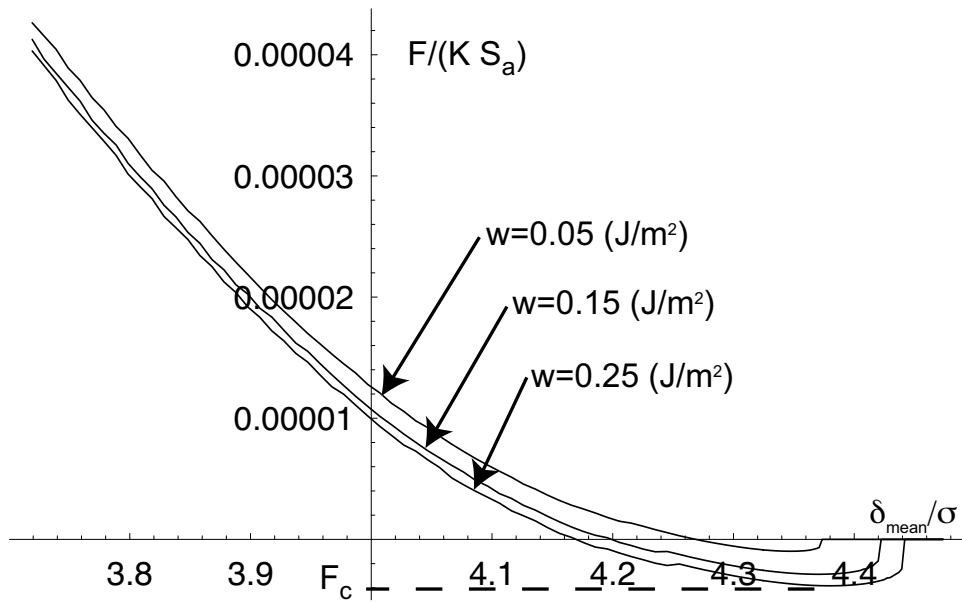


Figure 34: Effect of varying surface energy on adherence force.

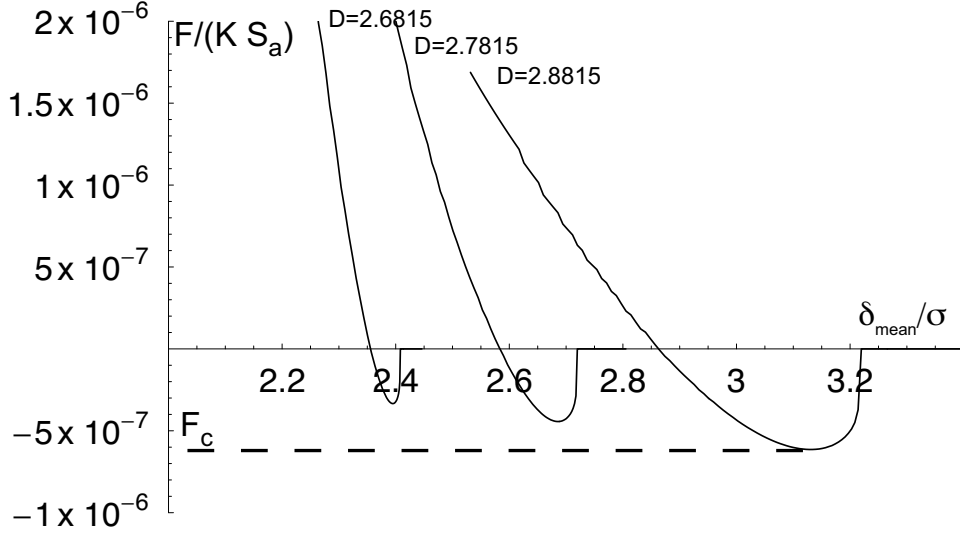


Figure 35: Effect of varying fractal roughness parameter  $D$  on adherence force.

work of adhesion,  $w$  (see Equation (1.1)).

As mentioned previously, surface roughness can have considerable influence on the adherence force. We will therefore consider the effect that varying the surface topography parameters  $D$  and  $G$  has on adherence of our system. Recalling its definition, as  $D$  increases, the surface becomes ‘smoother’, and the number of asperities increases. Based on this definition, it is not readily obvious what effect increasing  $D$  will have on adherence force. Figure (35) was plotted for our system to determine how the adherence force varies with  $D$ . In Figure (35), it is found that by slightly increasing  $D$ , the pull-off force can dramatically increase. One explanation for this fact is that a smoother surface interface will have a higher real to apparent contact area ratio. In such a condition, there is less disparity in asperity heights so that the compressive forces of the taller asperities do not dominate the adherence force.

Finally, considering the influence that the fractal scaling parameter  $G$  has on adherence in our system, the pull-off force was plotted in Figure (36) for different  $G$  values. From its definition, as  $G$  increases, the magnitude of the asperity peaks and become more pronounced. Thus, as shown in Figure (36), taller asperities are created as  $G$  increases which try to separate the interface, in effect reducing the pull-off force. From surface roughness results

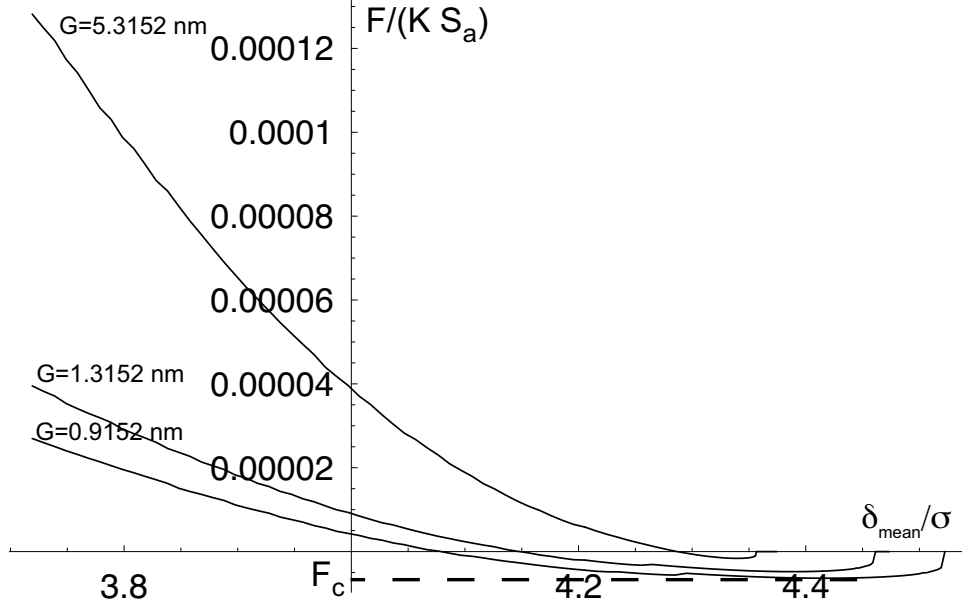


Figure 36: Effect of varying fractal scaling parameter  $G$  on adherence force.

in figures 35 and 36, it is readily apparent that another means of controlling the adherence force at a micro-sized contact interface is to control the surface topography, particularly the heights of the asperities.

## 5.5 CONCLUSIONS

A three-dimensional adhesive rough surface contact analysis was presented in this chapter. This numerical work provides a novel and computationally efficient method for analyzing contact between micro-scale components. Unlike many other adhesive rough surface contact solutions, no assumption has been made about the contact type prior to numerical integration. In the algorithm, the transition parameter is determined at the time of integration, thereby more accurately capturing the correct physics of the contact condition. To illustrate the applicability of the derived expressions, trends for controlling the adherence force for a LIGA nickel based system was examined. In the results, the parameters  $w$  and  $D$  are directly proportional to pull-off force, whereas  $K$  and  $G$  are found to be inversely propor-

tional to the adherence force. Furthermore, the proposed solution method can be used in conjunction with work of adhesion experiments to estimate the real area of contact. To date, work of adhesion values have either been determined by first principle calculations or have been presented as an ‘apparent’ work of adhesion. This brought about inaccuracies since the energy of adhesion was divided by the ‘apparent area’ rather than the real area of contact, this produces much lower values than calculated from first principle derivations. Since this solution offers a means of more accurately estimating the real area of contact and will more accurately approximate the experimentally determined value for the work of adhesion.

## 6.0 SCALE DEPENDENT ADHESIVE FRICTION MODEL

### 6.1 INTRODUCTION

In chapter 5, an adhesive rough surface solution was presented for surfaces that demonstrate multi-scale roughness behavior. In the present chapter, the total shear force during adhesive rough surface contact will be evaluated by combining the results of chapter 5 with a scale dependent friction model for single asperity contacts [38]-[39]. Hurtado and Kim (HK) in [38]-[39] developed a micro-mechanical dislocation model of frictional slip which consists of three distinct regimes which are determined by the area of contact for each asperity. Such a model is well suited for use with the fractal model presented in chapter 5 because of the multi-scale nature of the surface topography and contacts. Hence, the total friction force and coefficient of friction can be determined with respect to the fractal scaling and roughness parameters  $G$  and  $D$ .

### 6.2 HURTADO AND KIM MODEL

Based on dislocation theory, Hurtado and Kim (HK) have developed a scale dependent friction model. Their solution predicts the frictional forces to be determined in three different dislocation regimes. Johnson [40] provides an excellent description of these three regimes, which are based on the ratio of the contact radius,  $a$ , and the Burgers vector,  $b$ . The Burgers vector is the amount and direction of atomic displacement which will occur within a crystal when dislocation moves. For small contacts, where  $(a/b) < 30$ , HK theory shows that the shear stress,  $\tau_o$ , is constant and equal to the theoretical shear strength of a perfect crystal.

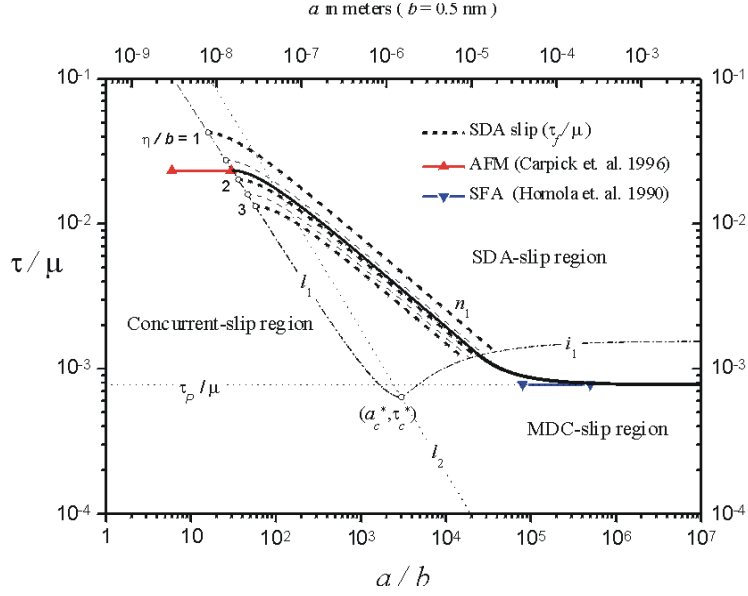


Figure 37: HK [39] scale dependent friction model.

For most materials, this is approximately  $G/30$ . For large contacts ( $a/b > 10^5$ ), Hurtado and Kim found that the frictional stress is constant and is equal to the Peierls stress. The Peierls stress is the minimal stress required for a dislocation movement at zero temperature. Finally, for intermediate contact sizes,  $30 < a/b < 10^5$ , HK theory finds that the frictional force is governed by the Peierls stress at the contact interface. These three regimes, which are shown in Figure (37), and will be described in more detail in the following sections.

### 6.2.1 CONCURRENT TO SINGLE-DISLOCATION-ASSISTED (SDA) SLIP

In the HK model, the first transition from small to intermediate sized contacts is commonly referred to as concurrent to SDA slip. At this first transition, the contact sizes are extremely small (on the order of 20 nm). For such a small contact size, a single dislocation loop is nucleated. In the case of concurrent slip the dislocation loop is defined by all of the atoms that are located within the contact radius,  $a$ . The nucleation sweeps across the entire contact area resulting in a slip displacement equal to  $b$ . In this regime, as the name suggests, all of the atoms move in a concurrent or a collaborative motion to move one lattice constant. In

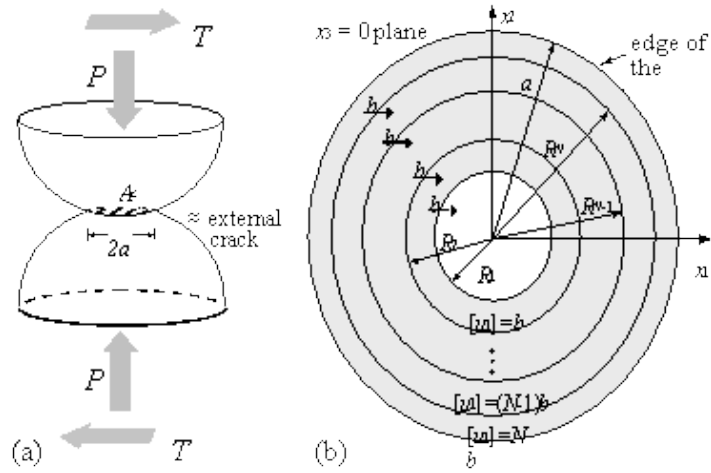


Figure 38: Model of dislocation loops. [39]

Figure (37), the experimental values in this regime were with an atomic force microscope. As illustrated in the figure, the slip that is taking place at the AFM tip is governed by ‘concurrent slip’. This transition leads into the new ‘transition regime’ of SDA slip where the contact sizes are typically on the order of 10 nm to 10  $\mu m$ , which is more typical in adhesive dry contacts [38]. As the contact sizes tend asymptotically smaller the shear strength becomes approximately  $G/30$ .

### 6.2.2 SDA SLIP TO MULTIPLE-DISLOCATION-COOPERATED (MDC) SLIP

In the SDA regime, the shear stress is governed by the force to nucleate one dislocation loop. As Johnson explains, the force required to nucleate one dislocation loop varies as  $a^{3/2}$ , and the stress varies as  $a^{-1/2}$ . Figure (37) shows the stress in the SDA regime varying with the contact radius as pointed out by Johnson. In the case when the contact size becomes larger, the frictional stress approaches the Peierls stress of the interface. In the second transition region from medium to large contacts, pile-up is modeled by several concentric dislocation loops (see Figure (38)). Johnson provides an excellent explanation of the transition that takes place at the transition between the SDA and MDC slip regions, “As the size of the

contact is increased, the dislocation loops equilibrate and pile up within the contact until a steady state is reached when the loops collapse at the same rate they are nucleated. This is the steady state regime in which the friction stress is constant and equal to the Peierls stress.”

### 6.3 HK IMPLEMENTATION

The implementation of the HK model will follow the work of Adams [41] who determined shear stress and coefficient of friction values using a statistical approach. Non-dimensionalization will be used in the form  $\bar{\tau}_f = \tau_f/G'$  where  $\tau_f$  is the frictional stress, and  $G'$  is the effective shear modulus given by:

$$G' = \frac{G_1 G_2}{G_1 + G_2}. \quad (6.1)$$

It is important to note in Figure (37) that the effective shear strength is written as ‘ $\mu$ ’, whereas the present investigation uses the symbol  $G'$ . The contact radius  $a$  is normalized by the Burgers vector  $b$ ,  $\bar{a} = a/b$ . As seen in Figure (37), the dimensionless shear stress can be written as a function of the dimensionless contact radius by the following condition:

$$\log(\bar{\tau}_f) = \begin{cases} \log(\bar{\tau}_{f_1}) & : \bar{a} < \bar{a}_1 \\ M \log(\bar{a}) + B & : \bar{a}_1 < \bar{a} < \bar{a}_2 \\ \log(\bar{\tau}_{f_2}) & : \bar{a} > \bar{a}_2 \end{cases} \quad (6.2)$$

where the parameters  $M$  and  $B$  are given by

$$M = -\log(\bar{\tau}_{f_1}/\bar{\tau}_{f_2})/\log(\bar{a}_2/\bar{a}_1) \quad (6.3)$$

$$B = \frac{(\log(\bar{\tau}_{f_1}) \log(\bar{a}_2) - \log(\bar{\tau}_{f_2}) \log(\bar{a}_1))}{\log(\bar{a}_2/\bar{a}_1)} \quad (6.4)$$

The force of friction can then be obtained by making the assumption that the friction force is directly proportional to the product of the shear stress and contact area,  $F_{fric} = \tau_f S$ . The resulting expression is non-dimensionalized and shown to have the following form:

$$\frac{F_{fric}}{G'b^2} = \begin{cases} \bar{\tau}_{f_1} \bar{a}^2 & : \bar{a} < \bar{a}_1 \\ 10^B \bar{a}^{M+2} & : \bar{a}_1 < \bar{a} < \bar{a}_2 \\ \bar{\tau}_{f_2} \bar{a}^2 & : \bar{a} > \bar{a}_2 \end{cases} \quad (6.5)$$

The above expressions are then implemented into the algorithm described in chapter 5. Each time the contact radius is determined for a particular asperity that is in contact, the scale-dependent friction regime can be then found. The resultant friction force for the  $i^{th}$  asperity is then added to the running sum. The friction force results have been computed and are presented in the following section.

## 6.4 RESULTS

Using the scale dependent HK friction model, results have been obtained for rough surface contact with multiple asperities. Because experimental parameters for the HK model are limited, the parameters have been taken from the literature [38], [39] and [41]. The model parameters utilized are:  $\bar{\tau}_{f_1} = 1/30$ ,  $\bar{\tau}_{f_2} = \bar{\tau}_{f_1}/43$ ,  $\bar{a}_1 = 28$ , and  $\bar{a}_2 = 80000$ . The effective shear modulus,  $G'$ , and Burgers vector,  $b$  are taken to be, 78.4 GPa and 0.249 nm respectively. In this section we will examine the effect of varying the fractal scaling,  $G$ , and roughness,  $D$ , parameters for the conditions given in Table 7.

For the purpose of understanding the effect of varying the fractal roughness parameter  $D$ , Figure (39) was generated. In the figure, it is found that the non-dimensional friction force is greater for lower  $D$  values at contact area ratios of 0.006 and higher. Consider  $S/S_{app} = 0.01$ , the non-dimensional friction values are 3200 for  $D = 2.6815$  and 3000 for  $D = 2.7815$ . Thus as the fractal roughness parameter increases the force of friction decreases. It is evident from this trend that surface roughness plays an integral role in determining friction at the micro-scale. To help explain the trend Equation (6.6) must be further examined. To quantitatively

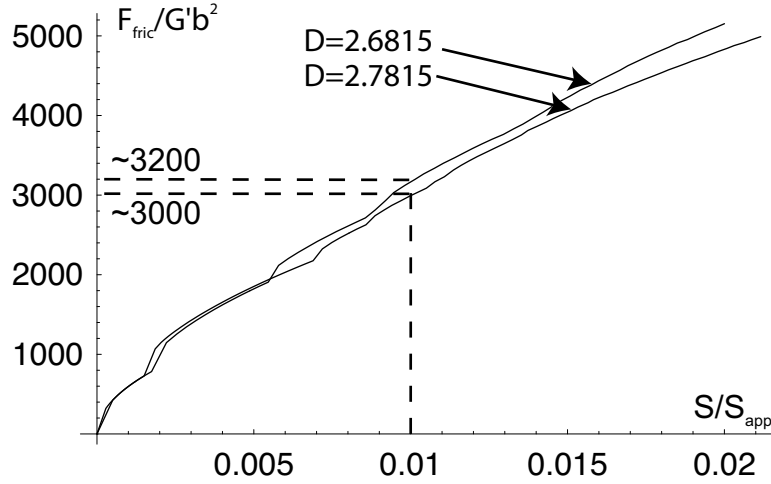


Figure 39: The effect of varying the fractal roughness parameter on friction.

verify that the roughness *does* vary with the fractal parameters, the following expression was derived by Majumdar [17] which relates the surface roughness to the fractal parameters:

$$\sigma = \sqrt{\frac{G^{2(D-1)}}{2 \ln \eta} \frac{1}{(4-2D)} \left( \frac{1}{\omega_l^{4-2D}} - \frac{1}{\omega_h^{4-2D}} \right)} \quad (6.6)$$

Using Equation (6.6) to determine the roughness, and Figure (39) to find the friction force, Table 8 was produced. Table 8 clearly shows a direct relationship between the friction force and the surface roughness. In Figure (39), if we consider a one percent contact for either  $D = 2.6815$  or  $2.7815$ , Table 8 shows that the surface roughness is increased by 216 percent and the non-dimensional friction force is increased by 6.6 percent. Therefore, Equation (6.6) verifies that as surface roughness is increased, the frictional force is expected to increase. Furthermore, two more trends are depicted in Figure (39): 1) below a value of 0.6 percent area of contact, the friction force is independent of surface roughness; 2) as the area of contact increases the percent increase in friction force increases.

To investigate the friction force relationship with the fractal scaling parameter,  $G$ , Figure (40) was generated. In the figure, the fractal scaling parameter is varied according to Table 7 and the effect on the total friction force is determined. In Figure (40) it is found that increasing the value of  $G$  decreases the friction. In this case, the correlation of surface

Table 8: The effect of varying  $D$  on friction force,  $G = 1.3152$  nm

Fractal parameters	$\sigma$	% Diff	$(F_{fric}/G'b^2)$	% Diff
$D = 2.6815$	39.3 nm	216	3200	6.6
$D = 2.7815$	16.5 nm		3000	

roughness and friction again holds true. Table 9 shows that for a thirty-three percent increase in surface roughness, an approximately two percent increase in the non-dimensional friction force is obtained. Figure (40) also illustrates that when the percent contact area becomes small, the difference in friction force is virtually negligible. In addition, in both figures 39 and 40, the relationship between friction and area is largely linear once the percent contact becomes greater than 0.6 percent.

## 6.5 DISCUSSION

By using this method described in this chapter, an experimental correlation could then be performed to approximate the real area of contact in MEMS components. Currently the experimental methods to determine the real area of contact are scarce. By implementing this scale dependent friction model into the adhesive rough surface contact algorithm developed in chapter 5, a unique method of combining the effects of adhesion, multi-scale surface roughness, and scale-dependent friction to approximate the true area of contact between interfaces. One could fit the model to the experimental results and would then have a method to predict the real area of contact for similar systems. It should be pointed out that when conducting friction experiments on a micro-scale, the total measured force applied by the experimenter is not a complete representation of the total normal force. Adhesion forces can be present which will alter the coefficient of friction estimate.

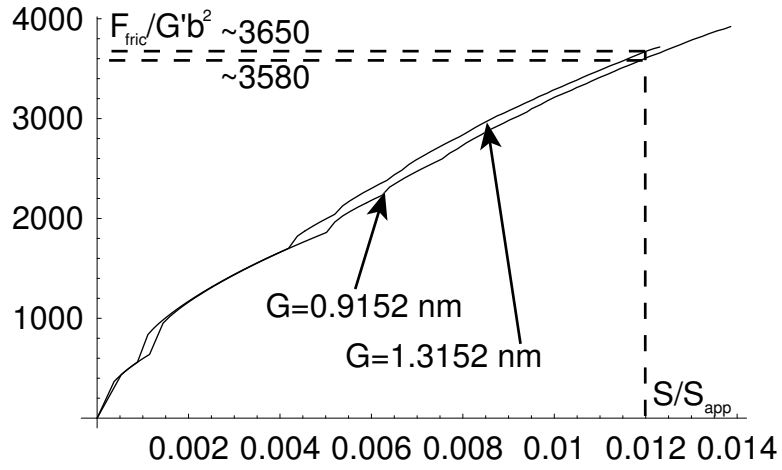


Figure 40: The effect of varying the fractal scaling parameter on friction.

Table 9: The effect of varying  $G$  on friction force,  $D = 2.7815$

Fractal parameter (nm)	$\sigma$	% Diff	$(F_{fric}/G'b^2)$	% Diff
$G = 0.9152$	12.4 nm	33	3580	1.95
$G = 1.3152$	16.5 nm		3650	

## APPENDIX

### CURVE-FIT EQUATIONS

$$\lambda = 5$$

$$A(\delta^*, \bar{\delta}^*) = 0.506581 + \sqrt{0.755717 + 0.82545(\delta^*/\bar{\delta}^*)} \quad (.1)$$

$$\bar{F}(\delta^*, \bar{\delta}^*) = -0.255531 - 1.72253A(\delta^*, \bar{\delta}^*)^2 + A(\delta^*, \bar{\delta}^*)^3 \quad (.2)$$

$$\lambda = 3$$

$$A(\delta^*, \bar{\delta}^*) = -0.408687 + 0.457199 \left( 1.92325 + \sqrt{3.69888 + 4(\delta^*/\bar{\delta}^*)} \right) \quad (.3)$$

$$\begin{aligned} \bar{F}(\delta^*, \bar{\delta}^*) = & 0.145313 - 2.15673(A(\delta^*, \bar{\delta}^*))^{1.04913} \\ & + 0.517717(A(\delta^*, \bar{\delta}^*))^{3.473} \end{aligned} \quad (.4)$$

$$\lambda = 2$$

$$A(\delta^*, \bar{\delta}^*) = 0.397699 + \sqrt{0.829211 + 0.879804(\delta^*/\bar{\delta}^*)} \quad (.5)$$

$$\begin{aligned} \bar{F}(\delta^*, \bar{\delta}^*) = & 0.0155519 - 2.13959(A(\delta^*, \bar{\delta}^*))^{1.0412656} \\ & + 0.593154(A(\delta^*, \bar{\delta}^*))^{3.346} \end{aligned} \quad (.6)$$

$$\lambda = 1.2$$

$$A(\delta^*, \bar{\delta}^*) = 0.230705 + \sqrt{0.968164 + 0.991943(\delta^*/\bar{\delta}^*)} \quad (.7)$$

$$\begin{aligned}\bar{F}(\delta^*, \bar{\delta}^*) &= -0.848921 - 1.52808(0.968164 + 0.991943(\delta^*, \bar{\delta}^*))^{0.492} \\ &\quad + 1.01187(0.968164 + 0.991943(\delta^*/\bar{\delta}^*))^{1.500}\end{aligned}\quad (.8)$$

$$\lambda = 1.0$$

$$A(\delta^*, \bar{\delta}^*) = 0.208561 + \sqrt{0.946903 + 0.963879(\delta^*/\bar{\delta}^*)}\quad (.9)$$

$$\begin{aligned}\bar{F}(\delta^*, \bar{\delta}^*) &= -0.990609 - 1.57412(0.946903 + 0.963879(\delta^*/\bar{\delta}^*))^{0.592} \\ &\quad + 1.1988699(0.946903 + 0.963879(\delta^*/\bar{\delta}^*))^{1.460}\end{aligned}\quad (.10)$$

$$\lambda = 0.7$$

$$A(\delta^*, \bar{\delta}^*) = 0.035611 + 1.02769(1.05759 + 1.07911(\delta^*/\bar{\delta}^*))^{0.488}\quad (.11)$$

$$\begin{aligned}\bar{F}(\delta^*, \bar{\delta}^*) &= -1.10144 - 1.26132(A(\delta^*, \bar{\delta}^*))^{1.203} \\ &\quad + 0.811666(A(\delta^*, \bar{\delta}^*))^{3.077}\end{aligned}\quad (.12)$$

$$\lambda = 0.5$$

$$A(\delta^*, \bar{\delta}^*) = 0.257819 + (0.974653 + 1.06842(\delta^*/\bar{\delta}^*))^{0.494}\quad (.13)$$

$$\begin{aligned}\bar{F}(\delta^*, \bar{\delta}^*) &= -1.34003 - 1.0821(A(\delta^*, \bar{\delta}^*))^{1.23} \\ &\quad + 0.901174(A(\delta^*, \bar{\delta}^*))^{3.0352}\end{aligned}\quad (.14)$$

$$\lambda = 0.1$$

$$A(\delta^*, \bar{\delta}^*) = 0.000620886 + \sqrt{0.4754718 + 1.0131375(\delta^*/\bar{\delta}^*)}\quad (.15)$$

$$\begin{aligned}\bar{F}(\delta^*, \bar{\delta}^*) &= -1.94645 - 0.375988(A(\delta^*, \bar{\delta}^*))^{2.0585} \\ &\quad + 1.11492(A(\delta^*, \bar{\delta}^*))^{2.957}\end{aligned}\quad (.16)$$

$$\lambda = 0.05$$

$$A(\delta^*, \bar{\delta}^*) = 0.000432064 + (0.335979 + 1.00369(\delta^*/\bar{\delta}^*))^{0.499}\quad (.17)$$

$$\begin{aligned}\bar{F}(\delta^*, \bar{\delta}^*) &= 0.997114(-1.98244 - 0.152864A(\delta^*, \bar{\delta}^*))^{1.571} \\ &\quad + A(\delta^*, \bar{\delta}^*)^{3.001}\end{aligned}\quad (.18)$$

## BIBLIOGRAPHY

- [1] K.L. Johnson. *Contact Mechanics*. Cambridge, UK, 1985.
- [2] K.N.G Fuller and D. Tabor. The effect of surface roughness on adhesion of elastic solids. *Proceedings of the Royal Society of London Series A*, 345:327–342, 1975.
- [3] K. Komvopoulos and W. Yan. Three-dimensional elastic-plastic fractal analysis of surface adhesion in microelectromechanical systems. *Journal of Tribology*, 120:808–813, 1998.
- [4] K.L. Johnson, K. Kendall, and A.D. Roberts. Surface energy and the contact of elastic solids. *Proceedings of the Royal Society of London Series A*, 324:301–313, 1971.
- [5] D. Maugis. Adhesion of spheres: The jkr-dmt transition using a dugdale model. *Journal of Colloid and Interface Science*, 150:243–269, 1992.
- [6] J.M. Baney and C.Y. Hui. A cohesive zone model for the adhesion of cylinders. *J. Adhesion Sci. Technol.*, 11:393–406, 1997.
- [7] B.V. Derjaguin, V.M. Muller, and Y.P. Toporov. Effect of contact deformations on the adhesion of particles. *Journal of Colloid and Interface Science*, 53:314–326, 1975.
- [8] D. Maugis. On the contact and adhesion of rough surfaces. *J. Adhesion Sci. Technol.*, 10:161–175, 1996.
- [9] C. Morrow, M.R. Lovell, and Xinguo Ning. A jkr-dmt transition solution for adhesive rough surface contact. *J. Phys. D: Appl. Phys.*, 36:534–540, 2003.
- [10] D. Tabor. Surface forces and surface interactions. *Journal of Colloid and Interface Science*, 58:2–13, 1977.
- [11] V.M. Muller, V.S. Yushchenko, and B.V. Derjaguin. On the influence of molecular forces on the deformation of an elastic sphere and its sticking to a rigid plane. *Journal of Colloid and Interface Science*, 77:91–101, 1980.
- [12] V.M. Muller, V.S. Yushchenko, and B.V. Derjaguin. General theoretical consideration of the influence of surface forces on contact deformations and the reciprocal adhesion of elastic spherical particles. *Journal of Colloid and Interface Science*, 92:92–101, 1983.

- [13] J.A. Greenwood and J.B.P. Williamson. Contact of nominally flat surfaces. *Proceedings of the Royal Society of London Series A*, 295:300–319, 1966.
- [14] D. Maugis. *Contact, Adhesion and Rupture of Elastic Solids*. Springer-Verlag, Berlin Heidelberg, 2000.
- [15] K.S. Kim, R.M. McMeeking, and K.L. Johnson. Adhesion, slip, cohesive zones and energy fluxes for elastic spheres in contact. *Journal of the Mechanics and Physics of Solids*, 46:243–266, 1998.
- [16] A. Majumdar and B. Bhushan. Role of fractal geometry in roughness characterization and contact mechanics of surfaces. *J. Tribology*, 112:205–216, 1990.
- [17] A. Majumdar. *Fractal surfaces and their Applications to Surface Phenomena*. PhD thesis, University of California, Berkley, 1989.
- [18] A. Majumdar and B. Bhushan. Fractal model of elastic-plastic contact between rough surfaces. *J. Tribology*, 113:1–11, 1991.
- [19] P. Sahoo and S.K.R. Chowdhury. A fractal analysis of adhesion at the contact between rough solids. *Proc. Instn. Mech. Engrs.*, 210:269–279, 1996.
- [20] C. Morrow and M.R. Lovell. Fractal model for adhesive contact of jkr type. *submitted to Journal of Physics D Applied Physics*, tbd:tbd, tbd.
- [21] P. Sahoo and S.K.R. Chowdhury. A fractal analysis of adhesive friction between rough solids in gentle sliding. *WEAR*, 253:924–934, 2002.
- [22] P. Sahoo and S.K.R. Chowdhury. A fractal analysis of adhesive wear at the contact between rough solids. *Proc. Instn. Mech. Engrs.*, 214:583–595, 2000.
- [23] S. Wang and K. Komvopoulos. A fractal theory of the interfacial temperature distribution in slow sliding regime: Part i- elastic contact and heat transfer. *Journal of Tribology*, 116:812–823, 1994.
- [24] K. Komvopoulos and W. Yan. A fractal analysis of stiction in microelectromechanical systems. *Journal of Tribology*, 119:391–400, 1997.
- [25] S. Wang and K. Komvopoulos. A fractal theory of the interfacial temperature distribution in slow sliding regime: Part ii-multiple domains, elastoplastic contacts, and applications. *Journal of Tribology*, 116:824–832, 1994.
- [26] B. Bhushan. *Introduction to Tribology*. John Wiley and Sons, 2002.
- [27] D. Avnir, D. Farin, and P. Pfeifer. Molecular fractal surfaces. *Nature*, 308:261–263, 1984.

- [28] A. Majumdar and C.L. Tien. Fractal characterization and simulation of rough surfaces. *Wear*, 136:313–327, 1990.
- [29] M.V. Berry and Z.V. Lewis. On the weierstrass-mandelbrot fractal function. *Proceedings of the Royal Society of London Series A*, 370:459–484, 1980.
- [30] B.B. Mandelbrot. *The Fractal Geometry of Nature*. Freeman, San Francisco, 1982.
- [31] K.L. Johnson and J.A. Greenwood. An adhesion map for the contact of elastic spheres. *Journal of Colloid and Interface Science*, 192:326–333, 1997.
- [32] K. Komvopoulos and N. Ye. Three-dimensional contact analysis of elastic-plastic layered media with fractal surface topographies. *Journal of Tribology*, 123:632–640, 2001.
- [33] M. Ausloos and D.H. Berman. Elastic-plastic contact model for bifractal surfaces. *Proceedings of the Royal Society of London Series A*, 400:331–350, 1985.
- [34] W. Yan and K. Komvopoulos. Contact analysis of elastic-plastic fractal surfaces. *Journal of Applied Physics*, 84:3617–3624, 1998.
- [35] E. Anguiano, M. Pancorbo, and M. Aguilar. Fractals in the natural and applied sciences. pages 37–46, 1994.
- [36] H.S. Cho, K.J. Hemker, K. Lian, J. Goettert, and G. Dirras. Measured mechanical properties of liga ni structures. *Sensors and Actuators A*, 103:59–63, 2003.
- [37] J.P. Hirth and J. Lothe. *Theory of Dislocations*. John Wiley and Sons, New York, 1982.
- [38] J.A. Hurtado and K-S Kim. Scale effects in friction of single-asperity contacts. i. from concurrent slip to single-dislocation-assisted slip. *Proceedings of the Royal Society of London Series A*, 455:3363–3384, 1999.
- [39] J.A. Hurtado and K-S Kim. Scale effects in friction of single-asperity contacts. ii. multiple-dislocation-cooperated slip. *Proceedings of the Royal Society of London Series A*, 455:3385–3400, 1999.
- [40] K.L. Johnson. The contribution of micro/nano-tribology to the interpretation of dry friction. *Proceedings of the Institution of Mechanical Engineers Part C-Journal of Mechanical Engineering Science*, 103:59–63, 2003.
- [41] G.G. Adams. A nano-scale multi asperity model for contact and friction. *ASME Journal of Tribology*, 125:700–708, 2003.